Article

Developmental Cell

PRG-1 Regulates Synaptic Plasticity via Intracellular PP2A/β1-Integrin Signaling

Highlights

- PRG-1 affects spine density and synaptic plasticity in a cell-autonomous fashion
- Cell-autonomous PRG-1 action is mediated via its intracellular C terminus (PRG-1^{CT})
- PRG-1^{CT} acts via protein phosphatase 2A (PP2A)/ITGB1 activation
- Pharmacological ITGB1 activation restores spine density and synaptic plasticity

Authors

Xingfeng Liu, Jisen Huai, Heiko Endle, ..., Thomas Deller, Robert Nitsch, Johannes Vogt

Correspondence

jisen.huai@unimedizin-mainz.de (J.H.), robert.nitsch@unimedizin-mainz.de (R.N.), johannes.vogt@unimedizin-mainz.de (J.V.)

In Brief

Postsynaptic PRG-1 controls lysophosphatidic acid (LPA) signaling at glutamatergic synapses via presynaptic LPA_2 receptors. Liu et al. demonstrate that PRG-1 also affects spine density and synaptic plasticity in a cell-autonomous fashion via protein phosphatase 2A (PP2A)/ITGB1 activation. In line with this, PP2A activation with FTY720 rescued spine density and LTP in PRG-$1^{-/-}$ animals.

Liu et al., 2016, Developmental Cell *38*, 275–290
August 8, 2016
http://dx.doi.org/10.1016/j.devcel.2016.06.019

CellPress

Developmental Cell
Article

PRG-1 Regulates Synaptic Plasticity via Intracellular PP2A/β1-Integrin Signaling

Xingfeng Liu,[1,8] Jisen Huai,[1,8,*] Heiko Endle,[1,8] Leslie Schlüter,[1] Wei Fan,[1] Yunbo Li,[1] Sebastian Richers,[1] Hajime Yurugi,[2] Krishnaraj Rajalingam,[2] Haichao Ji,[1] Hong Cheng,[1] Benjamin Rister,[1] Guilherme Horta,[1] Jan Baumgart,[1] Hendrik Berger,[1] Gregor Laube,[3] Ulrich Schmitt,[4] Michael J. Schmeisser,[5,6] Tobias M. Boeckers,[5] Stefan Tenzer,[2] Andreas Vlachos,[7,10] Thomas Deller,[7] Robert Nitsch,[1,9,*] and Johannes Vogt[1,9,*]

[1]Institute of Microanatomy and Neurobiology, University Medical Center, Langenbeckstrasse 1, 55131 Mainz, Germany
[2]MSU-FZI, Institute for Immunology, University Medical Center, Langenbeckstrasse 1, 55131 Mainz, Germany
[3]Institute for Integrative Neuroanatomy, CCO, Charité – University Medicine Berlin, Charitéplatz 1, 10117 Berlin, Germany
[4]Department for Psychiatry and Psychotherapy, University Medical Center, Untere Zahlbacher Street 8, 55131 Mainz, Germany
[5]Institute for Anatomy and Cell Biology, Ulm University, Albert-Einstein-Allee 11, 89081 Ulm, Germany
[6]Department of Neurology, Ulm University, Oberer Eselsberg 45, 89081 Ulm, Germany
[7]Institute for Clinical Neuroanatomy, Neuroscience Center, Goethe University Frankfurt, Theodor Stern Kai 7, 60590 Frankfurt am Main, Germany
[8]Co-first author
[9]Co-senior author
[10]Present address: Institute of Anatomy II, Faculty of Medicine, Heinrich-Heine-University, Moorenstrasse 5, 40225 Düsseldorf, Germany
*Correspondence: jisen.huai@unimedizin-mainz.de (J.H.), robert.nitsch@unimedizin-mainz.de (R.N.), johannes.vogt@unimedizin-mainz.de (J.V.)
http://dx.doi.org/10.1016/j.devcel.2016.06.019

SUMMARY

Alterations in dendritic spine numbers are linked to deficits in learning and memory. While we previously revealed that postsynaptic plasticity-related gene 1 (PRG-1) controls lysophosphatidic acid (LPA) signaling at glutamatergic synapses via presynaptic LPA receptors, we now show that PRG-1 also affects spine density and synaptic plasticity in a cell-autonomous fashion via protein phosphatase 2A (PP2A)/β1-integrin activation. PRG-1 deficiency reduces spine numbers and β1-integrin activation, alters long-term potentiation (LTP), and impairs spatial memory. The intracellular PRG-1 C terminus interacts in an LPA-dependent fashion with PP2A, thus modulating its phosphatase activity at the postsynaptic density. This results in recruitment of adhesome components src, paxillin, and talin to lipid rafts and ultimately in activation of β1-integrins. Consistent with these findings, activation of PP2A with FTY720 rescues defects in spine density and LTP of PRG-1-deficient animals. These results disclose a mechanism by which bioactive lipid signaling via PRG-1 could affect synaptic plasticity and memory formation.

INTRODUCTION

Spines are the principal sites of excitatory synaptic transmission, playing important roles in synaptic plasticity and memory formation (Sala and Segal, 2014). The formation and maintenance of spines is regulated by integrins, a family of heterodimeric extracellular matrix (ECM) receptors that span the cytoplasmic membrane (Luo et al., 2007). Upon activation, integrins reorganize the actin cytoskeleton (Ethell and Pasquale, 2005; Shi and Ethell, 2006), which is the primary structural basis of spines (Fischer et al., 1998). While a large number of integrin family members have been detected at dendritic spines, integrin subunits β1 and β3 have been directly shown to play a role in spine remodeling of hippocampal neurons (Shi and Ethell, 2006). Integrins most likely act in concert with other molecular regulators of spine plasticity (Ethell and Pasquale, 2005), which have been reviewed elsewhere (Bourne and Harris, 2008).

Plasticity-related gene 1 (PRG-1 or LPPR-4) is a member of an integral membrane protein family that possesses homology to the lipid phosphate phosphatases (LPPs) (Sigal et al., 2005). PRG-1 exhibits the characteristic LPP feature of three conserved domains facing the extracellular side of the plasma membrane, which enable LPPs to interact with bioactive lipid phosphates such as lysophosphatidate (LPA) or spingosine-1-phosphate (Brindley and Waggoner, 1998). Bioactive lipid phosphates initiate receptor-directed signaling cascades and regulate fundamental cellular processes (Moolenaar et al., 2004). PRG-1, however, interacts with LPA in a manner different from classical LPPs (McDermott et al., 2006) by enabling transmembrane transport of LPA to intracellular compartments (Trimbuch et al., 2009; Vogt et al., 2016). PRG-1 is expressed at postsynaptic sites of principal neurons and acts in a non-cell-autonomous fashion by controlling LPA in the synaptic cleft, which in turn stimulates presynaptic LPA receptors resulting in an increased release probability of glutamate vesicles at excitatory synapses (Tokumitsu et al., 2010; Trimbuch et al., 2009; Vogt et al., 2016). Previous studies have shown that various members of the PRG family play a role in regulating structural plasticity, including filopodia formation, neurite extension, and brain reorganization after lesion (Brauer et al., 2003; Broggini et al.,

2010; Coiro et al., 2014; Peeva et al., 2006; Savaskan et al., 2004; Sigal et al., 2007; Velmans et al., 2013). However, using ion-mobility enhanced data-independent label-free liquid chromatography (LC)-tandem mass spectrometry (MS), we have detected PRG-1 as a characteristic postsynaptic density (PSD) protein, while the other members of the PRG family were not found in a high-confidence PSD preparation (Distler et al., 2014). Interestingly, unlike other members of the type 2 phosphatidic acid phosphatase (PAP2) superfamily, PRG-1 contains an additional C-terminal hydrophilic domain of around 400 amino acids (aa) (Brauer et al., 2003). This domain has been shown to exhibit interaction motifs important for intracellular signaling cascades (Tokumitsu et al., 2010; Vogt et al., 2016), indicating an additional cell-autonomous function of PRG-1. Since (1) PRG-1 in the mouse brain is localized to the PSD of glutamatergic neurons, (2) its expression starts at embryonic day 19 (E19), and (3) it reaches its highest abundance in the third week of life (Brauer et al., 2003), i.e., during synaptogenesis and spine maturation, we hypothesized that PRG-1 could be involved in mediating these processes in a cell-autonomous fashion via its intracellular C terminus.

Since we detected an impact of PRG-1 on spine density and activation of β1-integrin, and found altered long-term potentiation (LTP) of excitatory synapses in PRG-1-deficient animals, we aimed to dissect the molecular signaling pathway that connects PRG-1 to β1-integrin activation and determine the importance of this pathway for synaptic plasticity and memory function.

RESULTS

PRG-1 Deficiency Reduced Hippocampal Spine Density and Impaired LTP

To address the role of PRG-1 in spine plasticity, we first compared spine densities in primary hippocampal neurons of wild-type (WT), PRG-1$^{-/-}$, and WT-overexpressing PRG-1 at 14 days in vitro (DIV) (Figures 1A–1C$_{1,2}$). Indeed, PRG-1$^{-/-}$ neurons showed a significant reduction in spine density of about 30% (Figure 1C$_1$), while overexpression of PRG-1 in WT neurons induced a significant increase in spine density, indicating a critical role of PRG-1 in spine formation and density. However, spine morphology, i.e., spine head area, was not affected (Figure 1C$_2$). Further assessment of the neuronal morphology revealed a decreased dendritic arborization (Figures 1D and 1E) in PRG-1$^{-/-}$ neurons, which mainly affected higher-order dendritic branches while not affecting the number of dendritic end tips per se (Figures S1A and S1B). To correlate these results with a functional readout for synaptic plasticity, we probed LTP at Schaffer collateral-CA1 synapses in acute slices prepared from WT and PRG-1$^{-/-}$ animals (Figure 1F). Impairment of LTP was observed in PRG-1$^{-/-}$ animals, and hence the results of these initial experiments point toward an important role of PRG-1 in regulating spine/synapse plasticity.

PRG-1 Expression Induces Specific Cell Adhesion

To uncover molecular pathways through which PRG-1 could affect plasticity, we performed experiments in non-neuronal cells, i.e., HEK-293, which do not express PRG-1 (Figure S1C). Interestingly, stably PRG-1-expressing HEK293 cells showed increased filopodia formation (Figure 1G) and higher vinculin expression (Figure 1H), a membrane-cytoskeletal protein involved in linking integrins to actin (Thompson et al., 2013), when compared with naive HEK293 cells. However, filopodia formation in PRG-1-expressing HEK293 cells was only observed in HEK293 cells expressing full-length PRG-1 but not in HEK293 cells expressing only the transmembrane part of PRG-1 (Figures S1E and S1F). These results indicate a role for PRG-1 in structural plasticity, which appears to be mediated by the intracellular PRG-1 C terminus. Interestingly, the function of the C terminus was only observed when it was an integral part of the PRG-1 molecule, and could not act on its own (Figure S1G). These findings are in line with increased spine numbers in PRG-1-overexpressing WT neurons and support the notion that PRG-1 is involved in mediating structural plasticity.

To understand whether this structural plasticity is accompanied by expression of molecules involved in cell adhesion, we used a crystal violet absorbance assay and analyzed binding to various components of the ECM. PRG-1 overexpression specifically increased binding to fibronectin (FN) and laminin (LN), but not to collagens, tenascin, or vibronectin (Figure 1I). Quantitative assessment of cell adhesion revealed a robust increase in binding of PRG-1-expressing HEK293 cells to FN-coated (Figures 1J and 1K) and LN-coated surfaces (Figures 1J and 1L), respectively. Since PRG-1 is an LPA-interacting molecule, we also tested for the effect of LPA on PRG-1-induced HEK-293 cell adhesion, finding that LPA significantly reduced PRG-1 specific cell adhesion while not affecting naive HEK293 cells (Figure 1M). We conclude from these experiments that PRG-1 expression mediates a specific molecular pathway involved in cell adhesion.

PRG-1-Induced Cell Adhesion Is Mediated by β1-Integrins

Selective binding to FN and LN indicated that integrins β1 (ITGB1)-containing heterodimers are involved in PRG-1-mediated cell adhesion (Delwel et al., 1994). Therefore, we performed fluorescence-activated cell sorting (FACS) analysis of PRG-1-expressing HEK293 cells and indeed detected an increase in active surface ITGB1. Interestingly, total surface ITGB1 was similar in PRG-1-expressing and naive HEK293 cells (Figures 1N and 1O). Moreover, PRG-1-expressing HEK293 cells displayed a significant increased affinity to echistatin (Figure 1P), a desintegrin family member binding to activated integrins (Monleon et al., 2005), further indicating increased surface expression of activated ITGB1. Specific binding of PRG-1-expressing HEK cells to FN were fully blocked by echistatin (Figure 1Q) as well as by the blocking antibody P5D2, which specifically targets activated ITGB1 (Lenter et al., 1993) (Figure 1R).

To finally establish a firm link between ITGB1 and PRG-1-induced cell adhesion, we used a cell line devoid of both ITGB1 expression (GD25) (Wennerberg et al., 1996) and PRG-1 (Figure S1D). Expression of PRG-1-only did not increase adhesion to FN-coated surfaces, while such an increase was observed after PRG-1 and ITGB1 transfection of GD25 cells (Figure 1S).

PRG-1 Deficiency Leads to Reduced Active ITGB1 on Hippocampal Neurons

We further assessed the expression of endogenous activated ITGB1 on primary neurons (Figure 1T$_1$). PRG-1$^{-/-}$ neurons

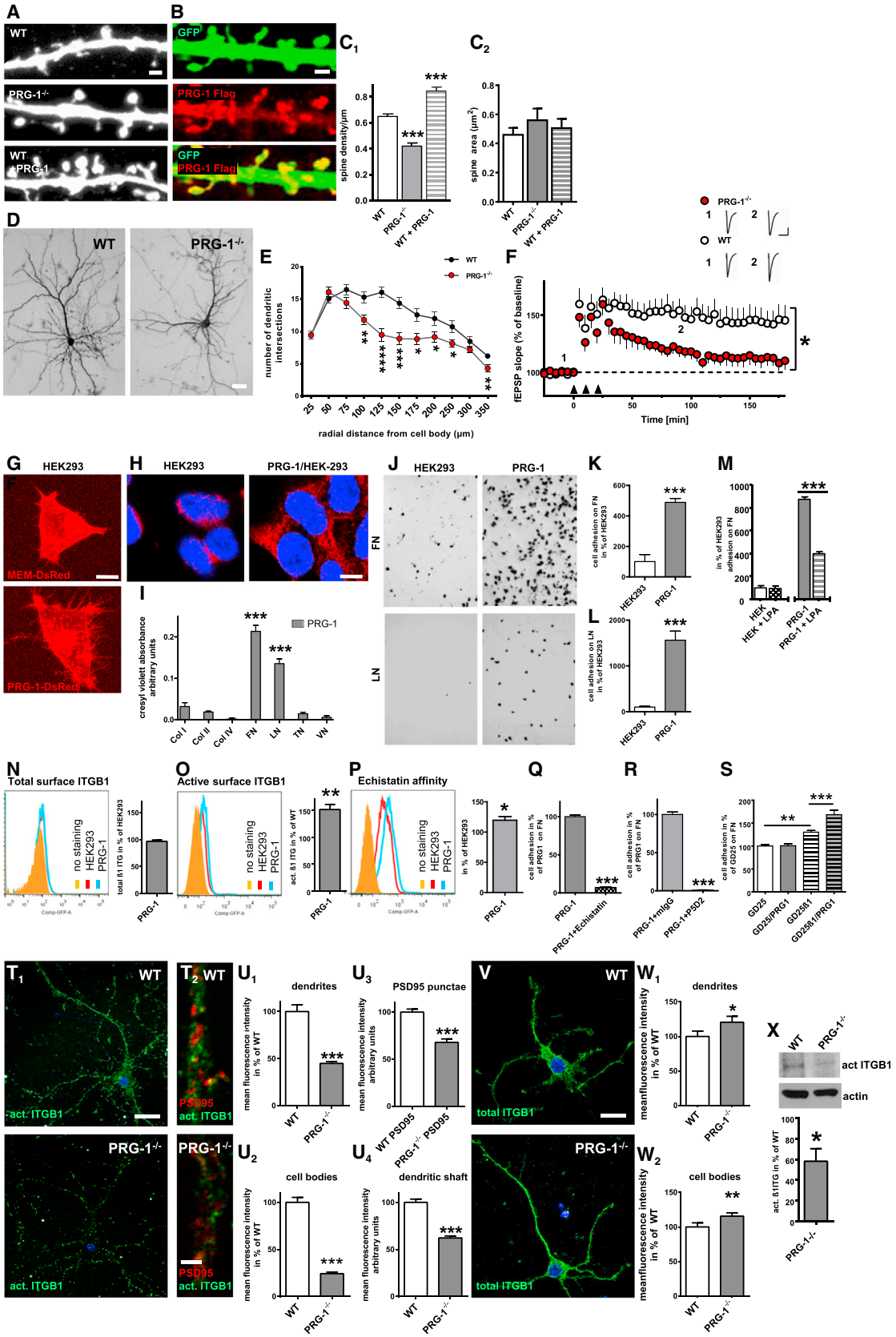

(legend on next page)

showed a strong reduction of activated ITGB1 signal on cell bodies and dendrites when compared with WT neurons (Figures 1U_1 and 1U_2). Signal intensity of clusters of activated ITGB1 was also reduced in PRG-1$^{-/-}$ in comparison with WT neurons (Figure S1J). Detailed analysis of active ITGB1 expression in the dendritic shaft and in the postsynaptic compartment (marked by PSD95) confirmed the specific decrease of active ITGB1 at synaptic sites in dendrites of PRG-1$^{-/-}$ neurons (Figures 1T_2, 1U_3, and 1U_4). Interestingly, expression of total ITGB1 was even slightly increased in neurons lacking PRG-1, indicating a specific role of PRG-1 in ITGB1 activation (Figures 1V, 1W_1, and 1W_2). Since we further confirmed the alteration of active ITGB1 using another independent method, i.e., hippocampal synaptic junction fractions of PRG-1-deficient mice (Figure 1X, see also Figure S1K for further information)—together with the results obtained in HEK293 cells—we are confident in concluding that PRG-1 is linked to the activation of ITGB1.

Direct Molecular Interaction of PRG-1 with PP2A, but not with ITGB1

Since our data so far provided strong evidence for a role of PRG-1 in ITGB1 activation, we assessed direct molecular interaction between both molecules. Using a proximity ligation assay (PLA) we detected a close vicinity of PRG-1 and ITGB1 in PRG-1-expressing HEK293 cells (Figures 2A and 2B). However, immunoprecipitation (IP) studies failed to demonstrate a direct interaction between PRG-1 and ITGB1 (Figure 2C). Therefore, we used ultra-performance LC-MS to identify other putative

Figure 1. Lack of PRG-1 Alters Spine Density and LTP while PRG-1 Expression Improves Cell Adhesion to Fibronectin and Laminin via Active Integrin β1 Upregulation

(A) Spine density in wild-type (WT) primary neurons, PRG-1$^{-/-}$, and WT neurons overexpressing PRG-1 (WT + PRG-1). Transfection with *GFP* or *PRG-1* was performed at 8 days in vitro (DIV) and imaging was performed at 14 DIV.

(B) Expression of PRG-1 fused to an FLAG tag reveals specific PRG-1 expression in dendritic spines.

(C_1 and C_2) Spine density was significantly decreased in PRG-1$^{-/-}$ neurons but increased in WT neurons after PRG-1 overexpression while spine area was not different between groups (Kruskal-Wallis with Dunn's multiple comparisons test; WT = 30 dendritic segments and 55 spines; PRG-1$^{-/-}$ = 19 dendritic segments and 41 spines; WT + PRG-1 = 29 dendritic segments and 54 spines).

(D and E) PRG-1$^{-/-}$ neurons at DIV 14 display a significantly decreased dendritic arborization (D) as shown by Scholl analysis (E, n = 19 WT and PRG-1$^{-/-}$ neurons, Mann-Whitney test; see also Figures S1A and S1B).

(F) Significantly decreased LTP in hippocampal CA1 of PRG-1$^{-/-}$ brain slices compared with WT controls (n = 13 WT and 13 PRG-1$^{-/-}$; two-way ANOVA; arrowheads indicate high frequency stimulation). Averaged excitatory postsynaptic potential (EPSP) samples during baseline (1) and 90 min post LTP induction (2) are shown above LTP graphs. Scale bars: x = 20 ms, y = 1 mV.

(G) Cellular protrusions and filopodia extending from PRG-1-DsRed expressing HEK293 cells (lower panel) compared with MEM-DsRed expressing controls (upper panel). See also Figures S1E–S1G.

(H) Increased focal adhesion formation in PRG-1-expressing cells shown by vinculin immunostaining.

(I) Cell adhesion on different ECM substrates (collagens I, II, and IV, fibronectin [FN], laminin [LN], tenascin [TN], vibronectin [VN]) were assessed via cresyl violet cell absorbance. Data were assessed after subtraction of unspecific adhesion on BSA-coated substrates (Kruskal-Wallis with Dunn's multiple comparisons post hoc, n = 6 experiments for each substrate).

(J–L) (J) Cell adhesion of naive and PRG-1-expressing HEK293 cells to FN- and LN-coated surfaces. Quantification is shown in (K) and (L) (FN, n = 9 experiments and LN, n = 6 experiments each, t test).

(M) Application of 1 μM LPA reduced adhesion of PRG-1-expressing HEK293 cells on FN but did not affect naive HEK293 cells (t test, n = 6 experiments per group).

(N and O) (N) FACS assessment of total surface integrin β1 (ITGB1; left, example of a flow cytometric assessment; right, quantification) revealed no difference between control HEK293 and PRG-1-expressing HEK293 cells while active ITGB1 was significantly higher in PRG-1-expressing HEK293 cells (O) (one-sample t test, n = 6 experiments per group).

(P) FACS assessment of cells incubated with fluorescent labeled echistatin (100 nM, 1 hr, left) shows significantly higher echistatin affinity of PRG-1-expressing HEK293 cells when normalized to the corresponding naive HEK293 cell values (one-sample t test, n = 5 experiments per group).

(Q) Quantification of cell adhesion of untreated and echistatin-pretreated (100 nM, 1 hr) PRG-1-expressing HEK cells on FN-coated plates (t test, n = 6 experiments per group).

(R) Quantitative assessment of cell adhesion of mIgG and P5D2-pretreated (active ITGB1-specific antibody, 2 μg/ml) PRG-1-expressing cells on FN-coated plates (t test, n = 6 experiments per group).

(S) Cell-adhesion assay using ITGB1-deficient GD25 cells. PRG-1 expression could only improve cell adhesion in the presence of ITGB1 (one-way ANOVA with Bonferroni post hoc, n = 6 experiments per group).

(T_1 and T_2) Immunostaining for active ITGB1 in WT and PRG-1$^{-/-}$ primary neurons (9 DIV; T_1). Active ITGB1 and PSD95 expression on WT and PRG-1$^{-/-}$ dendritic segments (9 DIV; T_2). Scale bars, 20 μm (T_1) and 1.5 μm (T_2).

(U_1–U_4) (U_1 and U_2) Mean fluorescence intensity of active ITGB1 was decreased in PRG-1$^{-/-}$ neuronal cell bodies and dendrites (since WT group was also used for analysis in Figures 3B and 3C, control for multiple comparisons was performed using one-way ANOVA with Bonferroni correction for parametric data and Kruskal-Wallis test with Dunn's multiple comparisons for non-parametric data; values are calculated in % of WT levels; n = 15 WT neuronal cell bodies and n = 9 PRG-1$^{-/-}$ neuronal cell bodies; n = 28 WT dendritic segments and 23 PRG-1$^{-/-}$ dendritic segments, see also Figure S1J). (U_3 and U_4) Significant reduction of active ITGB1 distribution in the dendritic shaft and postsynaptic compartment of PRG-1$^{-/-}$ neurons (n = 25 WT and 25 PRG-1$^{-/-}$ dendritic segments; t test; values are calculated in % of WT levels).

(V) Immunostaining for anti-integrin β1 (total ITGB1) shows comparable signal intensity in WT and PRG1$^{-/-}$ primary neurons (6 DIV).

(W_1 and W_2) Mean fluorescence intensity of cell bodies and dendrites of total integrin in PRG-1$^{-/-}$ neurons compared with WT (Mann-Whitney test, n = 40 neurons and dendrites and 43 PRG1$^{-/-}$ neurons and dendrites; values are calculated in % of WT levels).

(X) Synaptic junction fractions containing presynaptic and postsynaptic membranes revealed significant decrease of active ITGB1 in PRG-1$^{-/-}$ hippocampi compared with corresponding WT preparation (n = 6 experiments per genotype, one sample t test; see also Figure S1K).

Values represent mean ± SEM. *p < 0.05. **p < 0.01, ***p < 0.001, ****p < 0.0001. Scale bars represent 1.5 μm in (A) and (B), 20 μm in (D), 10 μm in (G) and (H), 1.5 μm in (T_2), and 20 μm in (T_1) and (V).

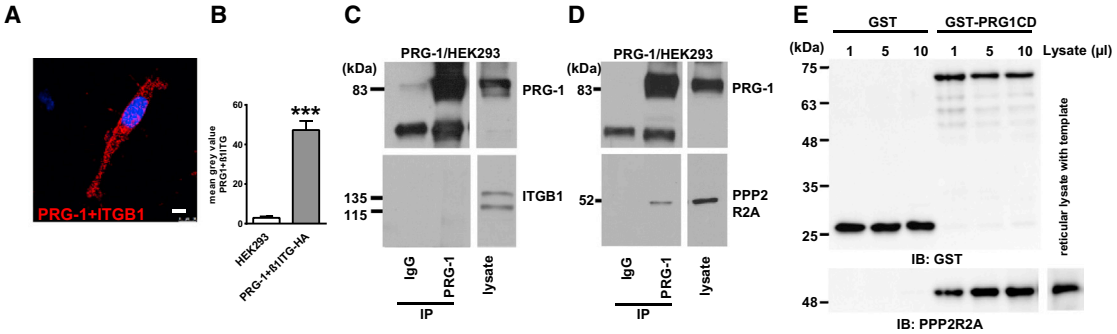

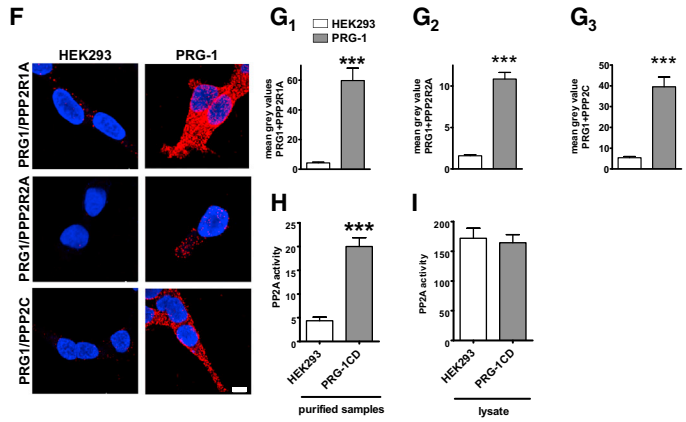

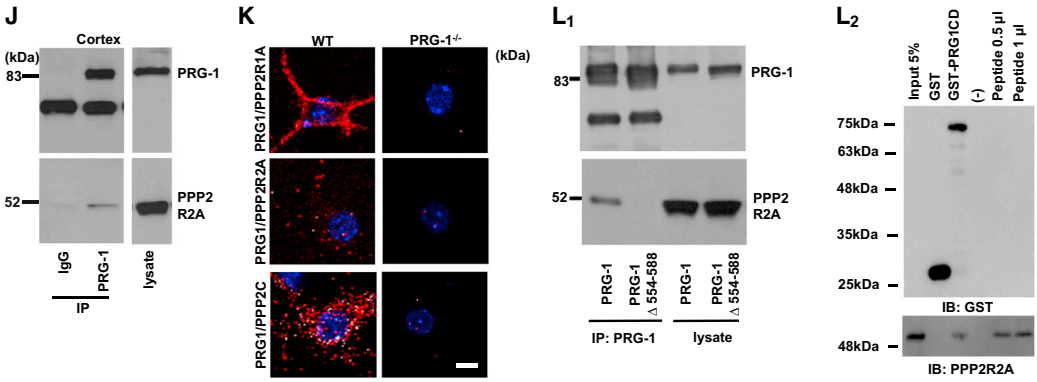

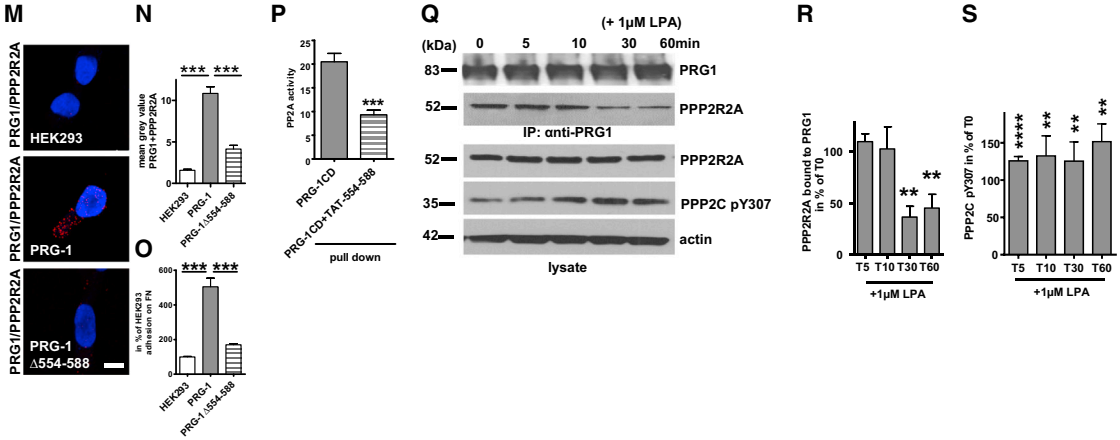

(legend on next page)

interaction partners of PRG-1 (Figures S2A and S2B) and confirmed a molecular interaction between PRG-1 and PPP2R2A using IP (Figure 2D). To provide evidence for a direct protein interaction, we expressed PPP2R2A in a cell-free system and performed in vitro pull-down experiments with the purified intracellular C terminus of PRG-1 bound to glutathione S-transferase (GST) (GST-PRG-1CD, see also Figures S2C and 2L_2). Our results strongly suggest a direct molecular interaction between both molecules (Figure 2E). In fact, PLA showed that this molecular interaction is accompanied by a close spatial vicinity of PRG-1 and the protein phosphatase complex PP2A, which is formed by PPP2R1A, PPP2R2A, and PPP2C (PLA, Figures 2F and 2G_1–2G_3). Using a pull-down assay to purify PPP2R2A bound to the cytoplasmic domain of PRG-1 in HEK293 cells, we detected significant phosphatase activity of this complex (Figures 2H and 2I), indicating functional relevance of the PRG-1/PP2A interaction at the membrane. Furthermore, using mouse cortical tissue, we confirmed an endogenous direct molecular interaction of PRG-1 with PPP2R2A (Figure 2J). In line with this, cortical neurons harbor PRG-1 and the protein phosphatase complex made up of PPP2R1A, PPP2R2A, and PPP2C in close spatial vicinity as shown by PLA (Figure 2K), indicating a role of this interaction in vivo.

Interaction with PP2A Requires aa 554–588 of the PRG-1 C Terminus

Besides other interaction partners, PP2A forms a complex with Ca^{2+}/calmodulin-dependent protein kinase IV (CaMKIV) (Westphal et al., 1998), and previous work by Tokumitsu et al. (2010) identified a calmodulin-binding motif in the intracellular C terminus of PRG-1 (at aa 554–588). We tested whether this motif is able to serve as a putative interaction site with PPP2R2A and analyzed HEK293 cells expressing a PRG-1 construct lacking this binding motif (PRG-1$^{\Delta 554-588}$, Figure 2L_1). IP studies showed no interaction between PRG-1$^{\Delta 554-588}$ and PPP2R2A (Figure 2L_1). Furthermore, by employing a short peptide of PRG1 (aa 554–588 coupled to TAMRA as a fluorescent dye), we demonstrated a direct interaction with PPP2R2A, thus confirming that this short aa stretch in the C terminus of PRG-1 is driving this interaction (Figures 2L_2 and S2E). PLA analysis also failed to reveal close spatial vicinity between PRG-1$^{\Delta 554-588}$ and PPP2R2A (Figures 2M and 2N). Consistent with these findings, HEK293 cells expressing PRG-1$^{\Delta 554-588}$ did not exhibit increased adhesion to FN, which was specific for cells expressing the WT PRG-1 construct (Figure 2O).

Application of the competitive peptide mimetic of the PRG-1 aa 554–588 fused to an HIV TAT cell penetrating sequence (TAT 554–588) to WT PRG-1-expressing HEK-293 cells significantly reduced phosphatase activity after pull-down of PRG-1 (Figure 2P). Taken together, this set of experiments suggest that the molecular interaction of PRG-1 and PPP2R2A at the 554–588 binding motif is a prerequisite for PRG-1 recruitment of active PP2A to the membrane. Since PRG-1 interacts with extracellular LPA (Brauer et al., 2003; Trimbuch et al., 2009; Vogt et al., 2016), we assessed the impact of LPA on HEK293 cells expressing PRG-1 (Figures 2Q–2S). These studies revealed that PRG-1/PPP2R2A interaction was decreased following LPA application (Figures 2Q and 2R) while phosphorylation of PPP2C at aa Y307 (as a marker for PP2A activity inhibition) was increased (Figures 2Q and 2S).

Figure 2. PRG-1 Interacts with PP2A

(A and B) (A) Proximity ligation assay (PLA) of *PRG-1* and *ITGB1* transfected cells indicating close vicinity of both molecules and a significant increase in PLA signal in PRG-1-expressing HEK293 cells (B; t test, n = 22 HEK-293 and n = 23 PRG-1-expressing HEK293 cells).

(C and D) Co-immunoprecipitation (IP) using a PRG-1 antibody shows PRG-1 and PPP2R2A association (D; see also Figures S2A and S2B), while no signal was detected for integrin β1 (ITGB1, C).

(E) IP using GST-coupled PRG-1 C-terminal domain (GST-PRG-1CD) produced in *E. coli* and PPP2R2A produced in a cell-free protein expression system. After in vitro reaction 1, 5, or 10 μl of the cell-free lysate was used as indicated. GST-coupled protein (upper panel) and PPP2R2A (bottom panel) detected by western blotting. Right panel shows the expression level of PPP2R2A from the rabbit reticulocyte lysate (see also Figures S2C and S2D).

(F and G) PP2A subunits A (PPP2R1A), B (PPP2R2A), and C (PPP2CA) were found in close proximity to PRG-1 in PRG-1-expressing HEK293 cells as shown by in situ PLA and fluorescence signal quantification (G_{1-3}; PPP2R1A n = 9 HEK and 8 PRG1; PPP2R2A n = 9 HEK and 11 PRG-1; PPP2CA n = 6 HEK and 9 PRG-1; n represents number of analyzed pictures. When more than one cell was visible, the mean of the displayed cells was calculated and used for the statistical analysis; t test was applied for parametric data and Mann-Whitney test was applied for non-parametric data).

(H) PP2A activity of tandem affinity purification pull-down from PRG-1CD (PRG-1 cytoplasmic domain) expressing cells and naive HEK293 cells assessed by a serine/threonine phosphatase assay shows significant increase of PP2A activity indicating maintained PP2A activity after recruitment by PRG-1 (t test, n = 6).

(I) PP2A activity in total cell lysates was not different in PRG-1CD expressing and naive HEK293 cells (t test, n = 6).

(J) IP using a PRG-1-specific antibody detected PRG-1/PPP2R2A interaction in the cortex.

(K) PP2A subunits A (PPP2R1A), B (PPP2R2A), and C (PPP2CA) were found in close proximity to PRG-1 in hippocampal neurons by PLA.

(L_1 and L_2) (L_1) Deletion of amino acids (aa) 554–588 of PRG-1CD impeded PRG-1 and PPP2R2A interaction as shown by IP using a PRG-1-specific antibody. (L_2) The PRG-1 aa 554–588 peptide tagged to TAMRA as a fluorescence indicator dye binds glutathione Sepharose (see also Figure S2E) and interacts with PPP2R2A produced in a highly standardized cell-free system.

(M and N) (M) PRG-1 aa 554–588 are critical for PRG-1/PPP2R2A interaction as shown by PLA and gray value quantification (N; since PRG-1/PPP2R2A group was also used in quantitative analysis shown in Figure 2G_2, control for multiple comparisons was performed by one-way ANOVA with Bonferroni post hoc correction, n = 9 for HEK-293 and n = 11 for PRG-1 and for PRG-1$^{\Delta 554-588}$-expressing HEK293 cells).

(O) Deletion of aa 554–588 significantly attenuated PRG-1-expressing cell adhesion on fibronectin-coated surfaces (one-way ANOVA with Bonferroni post hoc, n = 6 experiments per condition).

(P) PP2A activity of pull-down from PRG-1 CD-expressing HEK-293 cells and from TAT554-588-treated PRG-1-CD-expressing cells shows significantly lower activity than non-treated cells, indicating decreased PP2A/PRG-1 binding upon PRG-1CD/TAT554-558 interaction (t test, n = 6 for both groups).

(Q–S) (Q) Western blot of IP after LPA stimulation (1 μM) using a PRG-1 antibody indicates diminished PPP2R2A concentrations over time (R) and an increase of PPP2R2A phosphorylation (Y307) upon LPA stimulation (S; data normalized to the T0 values [set at 100] and calculated for each column using a one-sample t test; n = 6 experiments for PPP2R2A/PRG-1 association and n = 6 experiments for PP2ApY307).

Values represent mean ± SEM. **p < 0.01, ***p < 0.001, ****p < 0.0001. Scale bars, 10 μm.

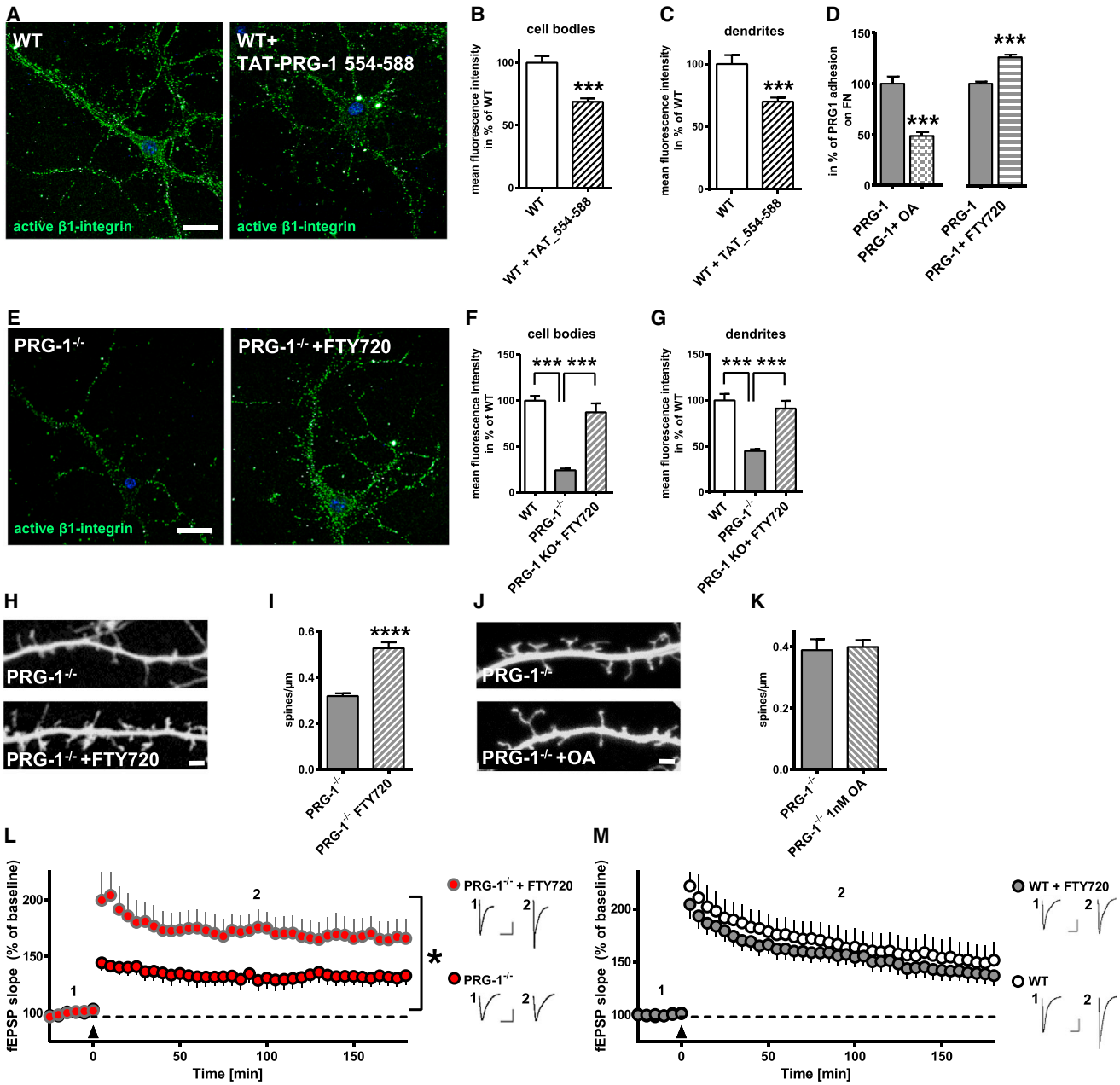

Figure 3. PRG-1/PP2A Interaction Induces ITGB1 Activation, Regulates Spine Density, and Enhances LTP

(A–C) (A) Active ITGB1 immunostaining of DIV9 WT hippocampal neurons treated with TAT-PRG-1-554-588 peptide (10 μM, 1 hr) display a significantly lower fluorescence intensity of active ITGB1 on neuronal cell bodies and dendrites (B and C; t test, for cell bodies WT n = 18, WT + TAT-PRG-1-554-588 n = 13; for dendrites WT n = 28, WT + TAT-PRG-1-554-588 n = 27). Scale bar, 20 μm.

(D) PP2A activator FTY720 (1 μg/ml, 1 hr preincubation) significantly improved cell adhesion while the PP2A inhibitor okadaic acid (OA) (100 nM, 2 hr preincubation) prevented PRG-1-dependent cell adhesion (t test, PRG-1, PRG-1 + OA n = 5 experiments per group; FTY720 n = 8 experiments per group).

(E–G) PRG-$1^{-/-}$ primary neurons (9 DIV) display a significantly higher fluorescence signal for active ITGB1 after stimulation with the PP2A activator FTY720 (1 μg/ml, 48 hr incubation; F and G, one-way ANOVA with Bonferroni post hoc for normal distributed data and Kruskal-Wallis with Dunn's multiple comparison test for non-parametric data; for cell bodies WT n = 15, PRG-$1^{-/-}$ n = 9, PRG-$1^{-/-}$ + FTY720 n = 13; for dendrites WT n = 28, PRG-$1^{-/-}$ n = 23, PRG-$1^{-/-}$ + FTY720 n = 23).

(H and I) FTY720 (100 nM) treatment for 6 days significantly increased spine density in dissociated PRG-$1^{-/-}$ neurons (n = 69 PRG-$1^{-/-}$ and 34 PRG-$1^{-/-}$ + FTY720 dendritic segments; t test). Scale bar, 1.5 μm.

(J and K) Vehicle-treated PRG-$1^{-/-}$ neurons and PRG-$1^{-/-}$ neurons treated for 24 hr with 1 nM OA showed no significant change in spine density.

(legend continued on next page)

Interaction of PRG-1 with PP2A Is Involved in Activation of ITGB1, Regulation of Spine Density, and LTP

Next, we investigated the role of the molecular interaction of PRG-1 with PPP2R2A for PRG-1-dependent activation of ITGB1 and regulation of dendritic spine density. We used the competitive binding peptide TAT 554–588 in primary hippocampal neurons (Figure 3A) and detected a significant reduction of activated ITGB1 on both cell bodies (Figure 3B) and dendrites (Figure 3C).

To test for the role of PPP2R2A in mediating PRG-1-dependent activation of ITGB1, we used established pharmacological tools to either stimulate or inhibit PP2A activity. Following treatment with FTY720, which serves as an activator of PP2A (Perrotti and Neviani, 2013), PRG-1-expressing HEK293 cells showed a significant increase in specific adhesion to FN-coated surfaces (Figure 3D). In contrast, selective inhibition of PP2A by nanomolar concentrations of okadaic acid (OA) (Takai et al., 1992) significantly decreased this adhesion (Figure 3D). Moreover, FTY720 was able to induce expression of activated ITGB1 (Figure 3E) on cell bodies and dendrites of PRG-1$^{-/-}$ hippocampal neurons to levels observed in WT neurons (Figures 3F and 3G). In line with these results, PRG-1$^{-/-}$ hippocampal neurons treated with 100 nM FTY720 over 8 days showed an increase in spine density compared with untreated control cells (Figures 3H and 3I). However, treatment of PRG-1$^{-/-}$ neurons with 1 nM OA did not alter spine density, further supporting specific PRG-1/PP2A interaction in spine formation (Figures 3J and 3K). Finally, in vivo treatment with FTY720 (5 mg/kg per day for at least 30 days) significantly rescued the deficit in LTP at Schaffer collateral-CA1 synapses in PRG-1$^{-/-}$ slices (Figure 3L), while having no effect on LTP in WT animals (Figure 3M).

PRG-1 Organizes the Focal Adhesion Complex in Lipid Rafts

PP2A is known to interact with src (Pradhan et al., 2010), a non-receptor tyrosine kinase, thereby controlling activation of integrins. To analyze whether scr is involved in PRG-1/PP2A interaction driving ITGB1-mediated adhesion, we analyzed PRG-1-induced adhesion to FN using a cell line devoid of src (SFY cells) (Klinghoffer et al., 1999), which shows no PRG-1 expression (Figure S3A). Overexpression of PRG-1 was only able to increase adhesion in SFY cells in the presence of src (Figures 4A and S3A), but not in normal, non-src-expressing SFY cells (Figure 4A), demonstrating a crucial role of src in the PRG-1-dependent ITGB1 activation. PLA studies (Figure 4B) revealed a close spatial vicinity of src and PRG-1 (Figure 4C), while the src inhibitor PP2 (Hanke et al., 1996) was able to block any PRG-1-mediated adhesion of HEK293 cells to FN (Figure 4D). Since PP2A and src can locate to lipid rafts (Xu et al., 2013), we analyzed whether PRG-1 has an impact on PPP2R2A and src in lipid rafts, and showed a significant PRG-1-dependent increase of both molecules in the lipid rafts containing membrane fraction (F2) (Figures 4E–4G).

To answer the question whether PRG-1 expression results in recruitment of further members of the focal adhesion complex important for ITGB1 activation to lipid rafts, we performed a systematic PLA study for ITGB1, talin (Calderwood, 2004), paxillin (Schaller, 2001), src, and PP2A in lipid rafts (identified by caveolin-1 expression) of PRG-1- and PRG-1$^{\Delta 554–588}$-expressing, and naive HEK293 cells (Figure 4H). We detected a significant increase in the presence of all the aforementioned molecular components in lipid rafts (Figures 4H and 4I). Importantly, the increase of their presence in lipid rafts was dependent on the direct molecular interaction of PRG-1 with PPP2R2A, since HEK293 cells expressing PRG-1$^{\Delta 554–588}$ lacking this interaction (Figure 2J) showed a significantly reduced lipid raft localization (Figures 4H and 4I).

The importance of the localization of this ITGB1 activating molecular complex in lipid rafts for PRG-1-induced adhesion of HEK293 cells to FN-coated surfaces was further demonstrated using MβCD and nystatin, known to disrupt raft formation (Wang et al., 2013), both of which were able to block this PRG-1-induced adhesion (Figure 4J). In fact, PLA studies (Figure 4K) revealed that PRG-1 is in close spatial vicinity to both talin and paxillin Figures 4L$_1$ and 4L$_2$). Seeding of PRG-1-expressing HEK cells on FN-coated surfaces in turn showed a time-dependent increase in paxillin phosphorylation (Figures 4M and 4N), indicating an outside-in signaling promoting paxillin action to stimulate focal adhesion complexes.

To understand the impact of PRG-1 on talin, we first assessed the total amount of talin and did not detect a difference between naive and PRG-1-expressing HEK cells (Figures 4O and 4P). FACS analysis revealed an increase in immunolabeling of talin rod and a decrease in talin head in PRG-1-expressing HEK293 cells when compared with their controls while no difference in serine-425 phosphorylation of talin could be observed (Figures 4Q and 4R). These data indicate that PRG-1 induces the talin head to form a complex with the ITGB1 cytoplasmic tail, thereby hiding the epitope for antibody binding.

PRG-1 Is Important for Hippocampal Spine Density In Vivo

Finally, we aimed to demonstrate the relevance of PRG-1 for the regulation of neuronal spine plasticity in vivo. Using electron microscopy, we detected that PRG-1 is already expressed in nascent spines at the PSD as early as P2, allowing for its involvement in spine formation (Figures S4A–S4D). Next, we assessed spine density in three different regions of the hippocampus (Figure 5A) at postnatal day 12 (P12) and P19 (Figures 5B and 5D). In all areas and at all time points investigated, our spine counts revealed significantly lower densities in PRG-1-deficient mice compared with WT littermate controls (Figures 5C and

(L) LTP in hippocampal CA1 of PRG-1$^{-/-}$ and FTY720-treated PRG-1$^{-/-}$ mice. Arrowhead indicates stimulation (n = 6 PRG-1$^{-/-}$ and 6 FTY720 treated PRG-1$^{-/-}$ mice; two-way ANOVA). Averaged EPSP samples during baseline (1) and 90 min post LTP induction (2) are shown to the right of LTP graphs. Scale bars: x = 20 ms, y = 0.25 mV.

(M) LTP in hippocampal CA1 of WT and FTY720-treated WT mice. Arrowhead represents stimulation (n = 10 WT and 10 FTY720-treated WT mice; two-way ANOVA). Averaged EPSP samples during baseline (1) and 90 min post LTP induction (2) are shown to the right of LTP graphs. Scale bars: x = 20 ms, y = 0.5 mV. Values represent mean ± SEM. *p < 0.05, ***p < 0.001, ****p < 0.0001. Scale bars represent 20 μm in (A) and (E) and 1.5 μm in (H) and (J).

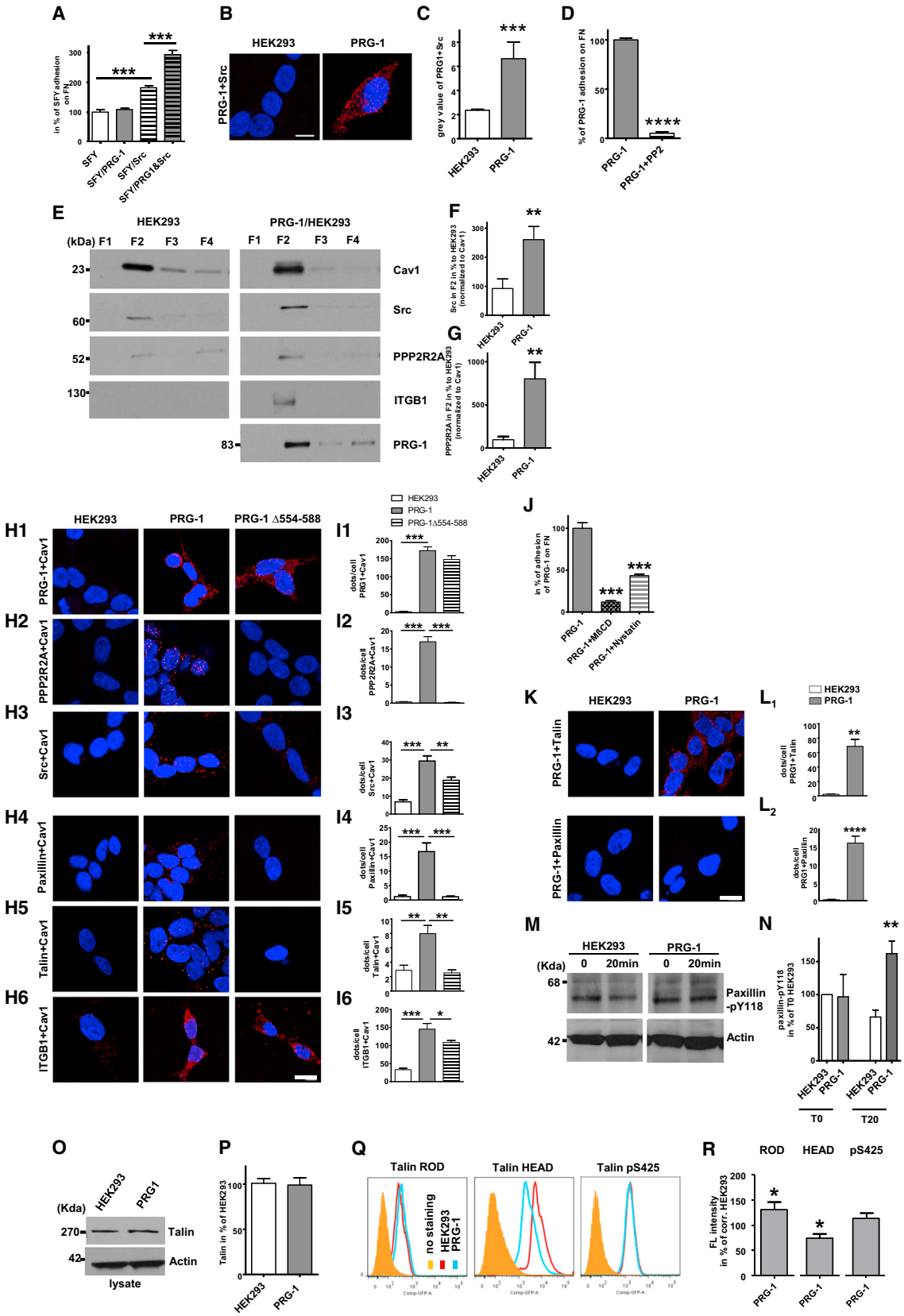

(legend on next page)

5E). To provide unequivocal evidence that spine density depends on postsynaptic PRG-1, we electroporated a *Cre*-encoding construct into the brain of mice carrying a floxed *prg-1* gene, thus deleting PRG-1 expression (Figure 5F). Similar to the results in the PRG-1$^{-/-}$ mice, single PRG-1-deficient neurons showed a highly significant decrease in their spine density compared with PRG-1-expressing neurons (Figures 5F and 5G).

Interestingly, in PRG-1$^{-/-}$ animals, active ITGB1 was no longer confined to dendritic spines as was the case in WT animals (Figures S4E–S4H). These findings support the hypothesis that postsynaptic PRG-1 directly modulates spine density via ITGB1. We further assessed whether the introduction of postsynaptic PRG-1 in a PRG-1$^{-/-}$ brain is sufficient to rescue the spine density. Spine analysis indeed confirmed that PRG-1 expression in single cells in a PRG-1$^{-/-}$ brain (Figure 5F) was able to reconstitute spine density in these neurons (Figures 5F and 5G). Since we have previously shown that PRG-1 modulated glutamatergic transmission in a non-cell-autonomous fashion via the presynaptic LPA_2 receptor (Trimbuch et al., 2009), we now analyzed whether a PRG-1 variant (PRG-1^{R346T}), not capable of intracellular LPA uptake (Vogt et al., 2016) and thereby unable to act in a non-cell-autonomous fashion, still has the capacity to affect spine density in PRG-1$^{-/-}$ animals. As shown in Figure 5F, in utero electroporation of *PRG-1^{R346T}* induced a visible increase in spine density resulting in a rescue to WT levels (Figure 5G).

To determine whether the observed decrease in spine density is transient and subsequently normalizes with brain maturation, we also analyzed spine densities in adult animals. We found that the highly significant reduction of spine density observed in the juvenile brain was still present in adults while other features of spine morphology were not altered (Figures 5H–5I$_2$). Quantification of VGlut1-positive axonal boutons impinging on dendritic shafts showed no differences between WT and PRG-1$^{-/-}$ neurons, while density of spine-associated VGlut1-positive boutons was drastically reduced (Figures S4I–S4K). This shows that decreased axonal contacts on spines are not compensated by shaft synapses. To assess a role of PRG-1 in the dynamic regulation of spine density, we either kept WT and PRG-1$^{-/-}$ animals in isolation or exposed them to an enriched environment. Assessment of spine density showed significant increase of spine density in WT animals under enriched conditions but no changes in PRG-1$^{-/-}$ animals, showing a loss of dynamic regulation of spine density in PRG-1$^{-/-}$ animals (Figure S4L).

PRG-1 Regulates Spine Plasticity and Spatial Memory in Cell-Autonomous Fashion

Our data so far indicate a cell-autonomous action of PRG-1 on spine density mediated by molecular interaction resulting in ITGB1 activation. However, PRG-1 plays a role in the modulatory control of hippocampal excitability in a non-cell-autonomous fashion (Trimbuch et al., 2009). Since spine density can be affected by neuronal activity (McKinney et al., 1999), we have addressed a role of altered neuronal activity observed in PRG-1-deficient animals (Trimbuch et al., 2009) on spine density. The non-cell-autonomous PRG-1 role in controlling excitability results in an increase in synaptic strength of PRG-1$^{-/-}$ animals (Trimbuch et al., 2009; Unichenko et al., 2016) and requires the presence of presynaptic LPA_2 receptor signaling (Trimbuch et al., 2009), and this hyperexcitability was fully reversed in LPA_2 receptor (LPA_2R)/PRG-1 double-deficient animals (Trimbuch et al., 2009). Hence, we tested for the possibility that alteration in spine densities can be explained by the LPA_2R-mediated non-cell-autonomous effect of PRG-1 on neural excitability and analyzed spine density in PRG-1-deficient animals on an $LPA_2R^{-/-}$ background (Figure 5J). While spine density analyses in $LPA_2R^{-/-}$ mice revealed no significant differences from WT animals, $LPA_2R^{-/-}$/PRG-1$^{-/-}$ animals displayed

Figure 4. PRG-1 and PP2A Organize Src/Paxillin/Tallin Complex Formation, Activating ITGB1

(A) Src-deficient cell line (SFY) showed PRG-1-specific cell adhesion only after Src expression (one-way ANOVA with Bonferroni post hoc, SFY and PRG-1/SFY n = 6, Scr/SFY n = 12, PRG-1/SRC/SFY n = 9 experiments per group; see also Figure S3A).

(B and C) (B) PLA showing in situ Src expression in close proximity to PRG-1. Quantification in (C) (t test, n = 6).

(D) Src inhibition via PP2 significantly reduced adhesion of PRG-1-expressing HEK293 cells to FN (t test, PRG-1 n = 6, PRG-1 + PP2 n = 8).

(E–G) (E) Western blot showing the F2 fraction of membrane rafts preparations from naive and PRG-1-expressing HEK293 cells. Upon PRG-1 expression (see clear band in the F2 fraction), signals for PPP2R2A, Src, and ITGB1 in the membrane raft fraction (F2) were markedly enhanced. Quantification of Src and PPP2R2A in (F and G) (F2, unpaired t test; for Src n = 8 and for PPP2R2A n = 6 experiments per group).

(H1–H6 and I1–I6) (H1, I1) PRG-1 (n = 6) and PRG-1$^{\Delta 554–588}$ (n = 6) show similar membrane raft localization as shown by colocalization with caveolin (Cav1) in the PLA. (H2, I2) PPP2R2A shows significantly higher membrane raft recruitment in PRG-1- (n = 7) but not in PRG-1$^{\Delta 554–588}$ (n = 7)-expressing cells. (H3–5, I3–5) Src (n = 9 for PRG-1 and n = 8 for PRG-1$^{\Delta 554–588}$), paxillin (n = 5 for PRG-1 and n = 6 for PRG-1$^{\Delta 554–588}$), and talin (n = 8 for PRG-1 and n = 6 for PRG-1$^{\Delta 554–588}$), which are located downstream of PPP2R2A, show significantly higher membrane raft recruitment in PRG-1 but not in PRG-1$^{\Delta 554–588}$-expressing cells. (H6, I6) Total ITGB1 expression in lipid rafts was significantly decreased in PRG-1$^{\Delta 554–588}$-expressing cells (n = 9) when compared with PRG-1-expressing cells (n = 10) (one-way ANOVA with Bonferroni post hoc for all experiments).

(J) Raft destruction by treatment with MβCD (5 mM, 30 min) or nystatin (25 μg/ml, 30 min) significantly reduced PRG-1-induced cell adhesion (one-way ANOVA with Bonferroni post hoc, n = 7 for PRG-1 and n = 6 for PRG-1 + MβCD or with nystatin).

(K and L) PLA showing expression of complex components for ITGB1 activation such as paxillin (n = 5 for HEK293 cells and n = 6 for PRG-1-expressing HEK293 cells) and talin (n = 5 for HEK293 cells and n = 8 for PRG-1-expressing HEK293 cells) in close proximity to PRG-1 (t test was used for parametric data, Mann-Whitney for non-parametric data).

(M and N) (M) Western blot showing paxillin phosphorylation (pY118) in naive and PRG-1-expressing HEK293 cells before (0 min) and 20 min after seeding on a fibronectin-coated plate. Quantification of gray values in (N) (normalized to T0 values of HEK293 cells) revealed significant increase of paxillin phosphorylation after 20 min in PRG-1-expressing HEK cells (one-sample t test for T0 of PRG-1 and unpaired t test for T20 of HEK-293 and PRG-1, n = 5 for all groups).

(O and P) (O) No difference in talin expression in western blot of cell lysate of naive and PRG-1-expressing HEK293 cells. Quantification is shown in in (P) (t test, n = 6 for all groups).

(Q and R) FACS analysis using antibodies against talin head, talin rod, and S425 talin phosphorylation. Quantification of talin rod (n = 6), talin head (n = 6), and serine-425 phosphorylation (n = 7) in PRG-1-expressing HEK293 cells in (R). (one-sample t test).

Values represent mean ± SEM. *p < 0.05. **p < 0.01, ***p < 0.001, ****p < 0.0001. Scale bars represent 10 μm in (B) and 20 μm in (H) and (K).

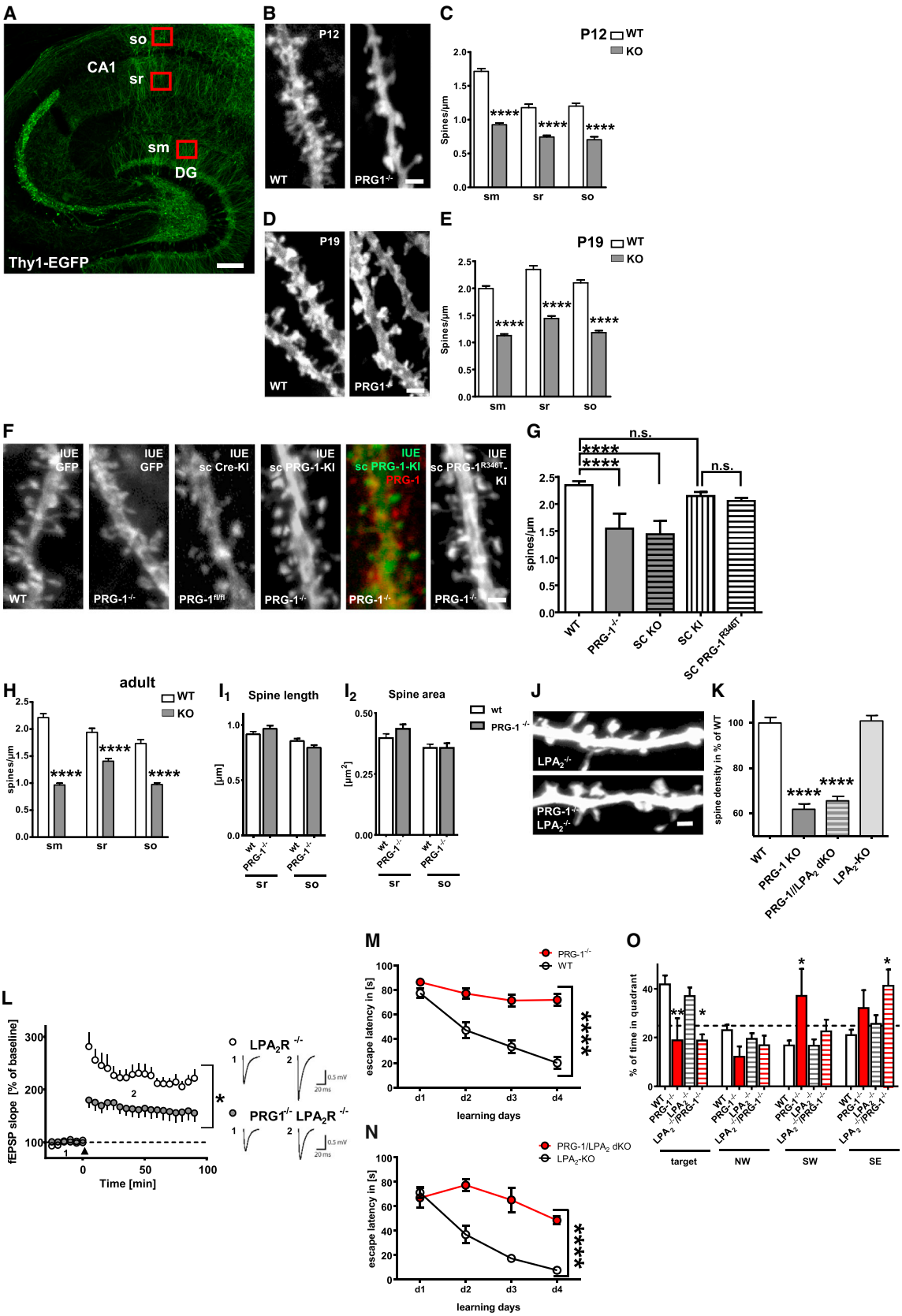

(legend on next page)

reduced spine densities (when compared with WT animals) which were not different to those seen in PRG-1$^{-/-}$ animals (Figures 5J and 5K). These LPA$_2$R$^{-/-}$/PRG-1$^{-/-}$ animals, with reduced spine density but no increase in synaptic strength, due to genetic ablation of the presynaptic LPA$_2$R mediating the increased synaptic strength in PRG-1$^{-/-}$ animals (Trimbuch et al., 2009), exhibit a reduction in LTP when compared with LPA$_2$R$^{-/-}$ animals, which lack the non-cell-autonomous action of PRG-1 mediated via presynaptic LPA receptors (Trimbuch et al., 2009), but maintain the cell-autonomous function mediated by the intracellular C terminus of PRG-1 at the postsynaptic side (Figure 5L). Taken together, these findings provide additional evidence for the fact that reduced spine plasticity in PRG-1$^{-/-}$ mice is not mediated by its non-cell-autonomous action regulating hyperexcitability via presynaptic LPA receptors, but rather depends on the ability of PRG-1 to induce a cell-autonomous intracellular signaling pathway upon LPA interaction mediated via the PRG-1 intracellular C terminus.

Finally, we carried out behavioral experiments using a Morris water maze (MWM) to test whether the observed deficits in spine density and LTP in the hippocampus of PRG-1$^{-/-}$ mice translate to alterations in spatial memory. PRG-1$^{-/-}$ mice showed a significantly lower performance in the learning phase and no significant spatial memory formation in the probe trial (Figures 5N and 5M). We also used LPA$_2$R$^{-/-}$/PRG-1 mice to rule out a non-cell-autonomous role of PRG-1 mediated by presynaptic LPA$_2$-Rs. Indeed, deficits in spatial memory observed in PRG-1$^{-/-}$ mice were not rescued by additional deletion of the presynaptic LPA$_2$ receptor (Figures 5M–5O), confirming a direct, cell-autonomous function of PRG-1 in these features.

DISCUSSION

In this study we report a physiological role of PRG-1 for neuronal spine density, LTP, and spatial memory. We demonstrate that PRG-1$^{-/-}$ mice have reduced spine density compared with their WT littermates. Spine density could be recovered by interfering with a signaling pathway by which a specific intracellular PRG-1 domain, via direct interaction with PPP2R2A, resulted in activation of ITGB1. This PRG-1 action is independent of its known extracellular role in controlling LPA receptor-mediated synaptic hyperexcitability (Trimbuch et al., 2009; Unichenko et al., 2016), and essential for proper spatial memory. These data provide evidence for the fact that PRG-1 controls hippocampal synaptic plasticity that is important for related memory function in a cell-autonomous fashion.

It is well established that actin rearrangement drives the formation and loss of dendritic filopodia, which are developmental precursors of spines (Ziv and Smith, 1996). This led us to hypothesize that molecular interaction occurring at the long cytoplasmic C terminus of PRG-1 influences actin regulatory proteins in an as yet unknown, cell-autonomous manner. Here we show that PRG-1 controls spine density via interaction of its cytoplasmic calmodulin-binding domain (CBD; Tokumitsu et al.,

Figure 5. PRG-1$^{-/-}$ Animals Display Decreased Spine Density and Altered Spatial Memory

(A) Hippocampus of a Thy-1 L21 EGFP mouse showing areas of spine assessment (highlighted by red squares): stratum radiatum (sr, apical dendrites) and stratum oriens (so, basal dendrites) of the CA1 region, and the outer two-thirds of stratum moleculare (sm) of the dentate gyrus (DG).

(B–E) (B and D) Spine density at P12 and P19 indicate lower spine density in PRG-1$^{-/-}$ mice at P12 (C, n = 16 WT and 37 PRG-1$^{-/-}$ for sm; n = 35 WT and 35 PRG-1$^{-/-}$ for sr; n = 35 WT and 33 PRG-1$^{-/-}$ for so) and at P19 (E, n = 23 WT and 33 PRG-1$^{-/-}$ for sm; n = 18 WT and 26 PRG-1$^{-/-}$ for sr; n = 21 WT and 21 PRG-1$^{-/-}$ for so; n represents analyzed dendritic segments; t test).

(F) Images of dendritic segments of an in utero *GFP*-transfected WT neuron and a constitutive PRG-1$^{-/-}$ neuron, of a single-cell PRG-1$^{-/-}$ neuron induced by *Cre*-electroporation in a PRG-1$^{flox/flox}$ brain (single-cell cre knockin, scCre-KI) and of a PRG-1 reconstituted neuron in a PRG-1$^{-/-}$ brain (scPRG-1-KI) with corresponding immunostaining for PRG-1, confirming effective PRG-1 re-expression, and of a PRG-1^{R346T} reconstituted neuron in an PRG-1$^{-/-}$ brain (from left to right).

(G) Single-cell PRG-1 deletion (scCre-KI) via in utero electroporation of a *Cre*-encoding construct in a conditional PRG-1$^{fl/fl}$ mouse showed a spine density reduction similar to that in PRG-1$^{-/-}$ animals. Re-expression of PRG-1 (scPRG-1 KI) rescued spine density in PRG-1$^{-/-}$ neurons to WT levels. A function-deficient PRG-1 variant (PRG-1^{R346T}), unable to take up LPA, also rescued density, pointing to PRG-1's cell-autonomous effect (n = 18 for WT, n = 20 for PRG-1$^{-/-}$, n = 26 for single-cell PRG-1$^{-/-}$, n = 13 for single-cell PRG-1-reconstitution (KI), and n = 18 for PRG-1^{R346T} reconstituted PRG-1$^{-/-}$ neurons; n represents analyzed dendritic segments; one-way ANOVA with Bonferroni post hoc).

(H) Adult PRG-1$^{-/-}$ animals displayed significantly reduced spine densities in all analyzed regions (n = 18 WT and 35 PRG-1$^{-/-}$ for sm; n = 17 WT and 23 PRG-1$^{-/-}$ for sr; n = 19 WT and 32 PRG-1$^{-/-}$ for so; n represents analyzed dendritic segments; t test; see also Figures S4I–S4K).

(I_1 and I_2) Spine length and spine head area were not altered in adult CA1 hippocampal neurons. n = mean of spine length in 36 dendritic segments for WT and of 55 dendritic segments for PRG-1$^{-/-}$ neurons. Spine area was measured in n = 207 spines of WT neurons and in 202 spines of PRG-1$^{-/-}$ neurons. Data were calculated using a t test or a Mann-Whitney test.

(J and K) (J) Dendrite of a LPA$_2$ receptor-deficient (LPA$_2$R$^{-/-}$) and a PRG-1$^{-/-}$/LPA$_2$R$^{-/-}$ CA1 pyramidal neuron. Quantitative analysis (K) shows significantly lower spine density in PRG-1$^{-/-}$ and PRG-1$^{-/-}$/LPA$_2$R$^{-/-}$ but not in LPA$_2$R$^{-/-}$ neurons (n = 51 for WT, n = 43 for PRG-1$^{-/-}$, n = 58 for PRG-1$^{-/-}$/LPA$_2$R$^{-/-}$, and n = 66 for LPA$_2$R$^{-/-}$; n represents analyzed dendritic segments; one-way ANOVA with Bonferroni post hoc).

(L) LTP in hippocampal CA1 of LPA$_2$-R$^{-/-}$ and LPA$_2$-R$^{-/-}$/PRG-1$^{-/-}$ mice. Arrowhead represents stimulation (n = 7 LPA$_2$-R$^{-/-}$ slices and n = 6 LPA$_2$-R$^{-/-}$/PRG-1$^{-/-}$ slices; two-way ANOVA). Averaged EPSP samples during baseline (1) and 45 min post LTP induction (2) are shown to the right of LTP graphs. Scale bars: x = 20 ms, y = 0.5 mV.

(M) Spatial memory in the Morris water maze was significantly decreased in PRG-1$^{-/-}$ mice when compared with WT litters (n = 19 WT and n = 12 PRG-1$^{-/-}$ mice; two-way ANOVA).

(N) PRG-1-expressing, LPA$_2$R$^{-/-}$ animals revealed a typical learning behavior but a significantly decreased learning by additional PRG-1 deletion (PRG-1$^{-/-}$/LPA$_2$R$^{-/-}$) (n = 11 LPA$_2$R$^{-/-}$ and n = 6 PRG-1$^{-/-}$/LPA$_2$R$^{-/-}$ mice; two-way ANOVA).

(O) Probe trials show that PRG-1$^{-/-}$ and PRG-1$^{-/-}$/LPA$_2$R$^{-/-}$ spent significantly less time in the quadrant that previously contained the platform than WT and LPA$_2$R$^{-/-}$ mice, indicating altered spatial memory in PRG-1$^{-/-}$ and PRG-1$^{-/-}$/LPA$_2$R$^{-/-}$ mice. Dotted line represents chance level (25%) (n = 18 WT, n = 10 PRG-1$^{-/-}$, n = 11 LPA$_2$R$^{-/-}$ and n = 6 PRG-1$^{-/-}$/LPA$_2$R$^{-/-}$ mice; Kruskal-Wallis with Dunn's multiple comparisons test was used for non-parametric data [target] and one-way ANOVA with Bonferroni post hoc was used for normally distributed data).

Values represent mean ± SEM. *p < 0.05, **p < 0.01, ****p < 0.0001; n.s., not significant. Scale bars represent 150 μm in (A) and 1 μm in (B), (D), (F), and (J).

2010) with the PP2A holoenzyme to activate ITGB1. PP2A holoenzymes, a family of serine-threonine phosphatases involved in controlling a diverse array of cellular processes including cell adhesion, consist of three subunits. The catalytic subunit C and a structural subunit A form the PP2A core enzyme dimer, while the third subunit B is believed to recruit the core enzyme dimer to form the holoenzyme and direct its localization to a particular subcellular compartment and, hence, modulate substrate selectivity and catalytic activity. To date, four unrelated families of B subunits have been identified: B/B55/PR55/PPP2R2, B′/B56/PR61/PPP2R5, B″/PR72/PPP2R3, and B‴/PR93/SG2NA/PR110/Striatin (Lambrecht et al., 2013). We found that PRG-1 itself is localized in plasma membrane rafts and acts as a scaffolding molecule to organize integrin adhesome assembly via its CBD associated with PPP2R2A (PPP2R2 isoform 1) and accordingly the holoenzyme. The molecular interaction between PRG-1 CBD and PP2A seems to be critical for organization of the adhesome, since disruption of this interaction by CBD deletion from PRG-1 also abolished the association of PRG-1 with other important adhesome components such as src, talin, and paxillin. Importantly, ITGB1 was also shown to be recruited to membrane rafts in a PRG-1-dependent fashion and, in line with present data on the adhesome components described here, all molecules were identified in a comprehensive proteome assessment of the PSD (Distler et al., 2014). These data indicate that the PRG-1/PP2A complex forms the core of the PRG-1-organized adhesome while the other components are attracted to proximity associated with the core and distributed around it to activate ITGB1.

It is known that integrin can be physically activated by talin binding to its cytoplasmic domain (Calderwood, 2004). Therefore, there is reason to assume that PRG-1 can activate ITGB1 via recruitment of talin through PP2A to the adhesome, and that ITGB1 itself is recruited to the proximity of membrane rafts where the PRG-1-organized adhesome further stimulates the activation of ITGB1 (Figure S5). Besides talin, src and PP2A were also reported to directly activate ITGB1 (Kim et al., 2004; Sakai et al., 2001). Furthermore, PP2A is able to stabilize ITGB1-mediated cell adhesion not only by dephosphorylation of ITGB1 but also by recruitment of IQGAP1 to ITGB1-Rac, thereby leading to ITGB1 anchoring to F-actin assemblies (Takahashi and Suzuki, 2006).

During neuronal development, spines are formed on dendrites reaching the highest density at the peak of synaptogenesis around the third week of rodent life. A generally accepted view is that neuronal activity modulates spine density, and recent findings show a direct correlation between spines and memory (Yang et al., 2009). This is in line with our findings in PRG-1$^{-/-}$ mice, which show decreased spine density and impaired spatial memory. Although the role of ITGB1 in spine development has been debated (Huang et al., 2006), recent data show that ITGB1 is critical in spine maturation (Bourgin et al., 2007; Ning et al., 2013). In line with their role for spine remodeling, integrins are critical for synaptic plasticity such as LTP, which is a correlate for memory formation (Chan et al., 2003). Further studies using knockout (KO) mice have identified integrins important for LTP and memory formation showing that ITGB1s (Chan et al., 2006; Huang et al., 2006) in combination with, e.g., α3-integrins (Chan et al., 2007; Kerrisk et al., 2013), are critically important for specific phases of LTP (Babayan et al., 2012; Chan et al., 2006; Huang et al., 2006). The downstream ITGB1 mechanism involves cofilin inactivation and actin polymerization (Wang et al., 2008). Our data provide evidence for the fact that the dynamics of spine formation as occuring under physiological conditions such as in an enriched environment is dependent on proper PRG-1/active ITGB1 signaling. The role for ITGB1 for dendritic spine plasticity, proper LTP induction, and hippocampal-dependent memory as described by previous work is in line with our data showing that activation of the PRG-1/PP2A/ITGB1 signaling is necessary for proper spine density and spatial memory.

AMPA (α-amino-3-hydroxy-5-methyl-4-isoxazolepropionic acid) receptors have been shown to play a role in spine growth and maintenance (McKinney et al., 1999), and activation of various NMDA (N-methyl-D-aspartic acid) receptors caused rapid spine retraction (Halpain et al., 1998). However, our own studies on PRG-1 do not provide evidence of changes in the classical molecular machinery at the synapse in PRG-1-KO mice. Immunofluorescent staining and western blot data on PSD-preparations showed no differences in the expression of presynaptic markers, such as synaptophysin, VGlut1, VGat, and GAD67, or postsynaptic markers, such as AMPA receptor subunits (GluR1, GluR2/3, GluR4), PSD-95, and the NMDA receptor subunits NR1 and NR2A/B in PRG-1$^{-/-}$ and their WT litters. Furthermore, the AMPA/NMDA ratio and the holding current changes on AMPA wash-in did not differ between the WT and PRG-1 KO mice (Trimbuch et al., 2009).

PRG-1 seems to act via LPA_2 receptors and has a modulatory role in excitatory transmission in a non-cell-autonomous fashion. Lack of postsynaptic PRG-1 has been shown to lead to an increased release of glutamate from the presynaptic axon terminal mediated via presynaptic LPA receptors (Trimbuch et al., 2009). We were able to rule out, however, that a loss of spines and alteration in synaptic plasticity as observed in the PRG-1-deficient mouse is due to increased synaptic activity. The fact that spine density, LTP, as well as spatial memory were not recovered in LPA_2/PRG-1 double-deficient mice, which exhibit normal synaptic activity (Trimbuch et al., 2009), provides evidence for a cell-autonomous action of PRG-1. In turn, genetically modified PRG-1 devoid of its LPA-uptake function but able to interact with PP2A (Trimbuch et al., 2009; Vogt et al., 2016), was still capable of mediating proper spine formation. This appears to be mediated via direct interaction of its intracellular C terminus with PPP2R2A and subsequent activation of ITGB1 regulating spine density.

Together with the functional and behavioral data, our molecular and morphological studies provide evidence for the fact that PRG-1 drives a cell-autonomous signaling pathway involved in the regulation of spine density, and subsequently memory formation.

EXPERIMENTAL PROCEDURES

DNA Constructs and Cell Lines, and Primary Neuronal Cultures

Constructs and establishment of stable expressing cell lines were obtained using standard procedures. GD25 cells were provided by Reinhard Faessler and MEF-SFY by Mirko Schmidt. Primary neuronal cultures were prepared as described by Vogt et al. (2012). For details see Supplemental Experimental Procedures.

Synaptic Junction Preparation

Synaptic junction fraction was isolated as described by Distler et al. (2014). For details see Supplemental Experimental Procedures.

Immunoprecipitation and Immunoblotting

Immunoprecipitation was performed according to standard procedures. Primary antibodies: PRG-1 (1:3,000, custom-made antibody against aa 624–637, NP_808332) (Trimbuch et al., 2009); ITGB1, PPP2R1A (81G5), PPP2R2A (100C1), PPP2C (52F8), Src (32G6), talin (C45F1), and paxillin pY118 (1:1,000), all from Cell Signaling; caveolin-1 (Cav1) (1:2,000) from Sigma; PPP2C pY307 (E155, 1:1,000) from Abcam; and β-actin (1:5,000) from MP Biomedicals. For details see Supplemental Experimental Procedures.

Flow Cytometry

Flow cytometry analyses were carried out on a FACS Canto II cytometer (BD Biosciences). Antibodies are described in detail in Supplemental Experimental Procedures.

Proximity Ligation Assay

PLA was performed using Duolink reagents (Sigma) according to standard protocols. Imaging was performed on the Leica platform of TCS SP8 confocal laser scanning microscope equipped with LAS AF software. For the evaluation of the specific number of dots per cell, pictures of representative cells with positive PLA were used.

Lipid Raft Preparation

Lipid rafts were extracted according to the instruction manual of Caveolae/Rafts Isolation Kit (Sigma).

Cell-Adhesion Assay

The cell-adhesion assay was adopted from the instruction manual of ECM Cell Adhesion Array Kit (Chemicon). For details see Supplemental Experimental Procedures.

Serine/Threonine Phosphatase Assay

Serine/threonine phosphatase studies were performed using a commercially available assay system (Promega).

In Utero Electroporation and Expression Plasmids for IUE

The in utero electroporation experiments were carried out as described by Trimbuch et al. (2009) in accordance with a protocol approved by the local animal welfare committee.

Immunofluorescence and Confocal Microscopy

Immunofluorescent staining of HEK-293 cells expressing PRG-1, PRG-1-FLAG, or primary neurons transfected with different constructs was performed as described elsewhere (Vogt et al., 2016). Antibodies are described in detail in Supplemental Experimental Procedures. Nuclear staining (DAPI; Invitrogen) was added for better visualization of HEK-293 cells and neurons.

Long-Term Potentiation

LTP was performed as described in Supplemental Experimental Procedures.

Morris Water Maze

All experimental procedures were carried out in accordance with the European Communities Council Directive regarding care and use of animals for experimental procedures and were approved by Landesuntersuchungsamt Koblenz, Germany.

Spatial learning and memory were tested by the MWM hidden platform task using the same maze and protocol as described in Supplemental Experimental Procedures.

Statistics

Data analysis was performed using GraphPad Prism 6 (GraphPad Software). After assessing for normal distribution (using the Kolmogorov-Smirnov test), data were analyzed using an unpaired two-tailed Student's t test for normally distributed data or a Mann-Whitney test for non-parametric data. Data normalized to control values (rendering control values as 100) were calculated using a one-sample t test. For comparison of multiple groups, normally distributed data were assessed using a one-way ANOVA with Bonferroni correction for multiple comparisons, or a Kruskal-Wallis test with Dunn's test for non-parametric data. For comparison of groups containing matched values (LTP + MWM) a two-way ANOVA was used. Differences were considered statistically significant at $p < 0.05$.

SUPPLEMENTAL INFORMATION

Supplemental Information includes Supplemental Experimental Procedures and five figures and can be found with this article online at http://dx.doi.org/10.1016/j.devcel.2016.06.019.

AUTHOR CONTRIBUTIONS

Conceptualization, R.N., J.H., and J.V.; Methodology, J.H., J.V., R.N., T.D., A.V., and K.R.; Investigation, X.L., L.S., Y.L., H.E., H.J., H.C., W.F., B.R., S.R., H.Y., G.L., S.T., J.B., H.B., M.J.S., G.H., G.L., T.M.B., and U.S.; Writing – Original Draft, R.N., J.H., and J.V.; Writing – Review and Editing, J.V. and R.N.; Supervision, R.N., J.H., J.V., and A.V.; Funding Acquisition, R.N., J.H., J.V., A.V., and T.D.

ACKNOWLEDGMENTS

We thank Darragh O'Neill for proofreading the manuscript, and Melanie Pfeifer and Nicolai Schmarowski for technical assistance. We further thank Reinhard Fässler, Mirko Schmidt, and Jerold Chun for providing cell lines and animals, respectively. Data from this study are part of the PhD thesis of X.L., the master's thesis of H.E., and the doctoral thesis of B.R. R.N., together with J.V., and T.D., together with A.V., dedicate this study to their mentor Michael Frotscher, who shaped their thinking on the intimate relation between structure and function in the nervous system. This work was supported by the Deutsche Forschungsgemeinschaft (SFB 1080) to R.N., J.V., J.H., A.V., and T.D. and the European Research Council (ERC-AG "LiPsyD") to R.N. K.R. is a Heisenberg Professor of the DFG (RA1739/4-1) and GFK, and a BIF-PLUS3 fellow.

Received: January 27, 2016
Revised: May 4, 2016
Accepted: June 14, 2016
Published: July 21, 2016

REFERENCES

Babayan, A.H., Kramar, E.A., Barrett, R.M., Jafari, M., Haettig, J., Chen, L.Y., Rex, C.S., Lauterborn, J.C., Wood, M.A., Gall, C.M., et al. (2012). Integrin dynamics produce a delayed stage of long-term potentiation and memory consolidation. J. Neurosci. *32*, 12854–12861.

Bourgin, C., Murai, K.K., Richter, M., and Pasquale, E.B. (2007). The EphA4 receptor regulates dendritic spine remodeling by affecting beta1-integrin signaling pathways. J. Cell Biol. *178*, 1295–1307.

Bourne, J.N., and Harris, K.M. (2008). Balancing structure and function at hippocampal dendritic spines. Annu. Rev. Neurosci. *31*, 47–67.

Brauer, A.U., Savaskan, N.E., Kuhn, H., Prehn, S., Ninnemann, O., and Nitsch, R. (2003). A new phospholipid phosphatase, PRG-1, is involved in axon growth and regenerative sprouting. Nat. Neurosci. *6*, 572–578.

Brindley, D.N., and Waggoner, D.W. (1998). Mammalian lipid phosphate phosphohydrolases. J. Biol. Chem. *273*, 24281–24284.

Broggini, T., Nitsch, R., and Savaskan, N.E. (2010). Plasticity-related gene 5 (PRG5) induces filopodia and neurite growth and impedes lysophosphatidic acid- and nogo-A-mediated axonal retraction. Mol. Biol. Cell *21*, 521–537.

Calderwood, D.A. (2004). Talin controls integrin activation. Biochem. Soc. Trans. *32*, 434–437.

Chan, C.S., Weeber, E.J., Kurup, S., Sweatt, J.D., and Davis, R.L. (2003). Integrin requirement for hippocampal synaptic plasticity and spatial memory. J. Neurosci. *23*, 7107–7116.

Chan, C.S., Weeber, E.J., Zong, L., Fuchs, E., Sweatt, J.D., and Davis, R.L. (2006). Beta 1-integrins are required for hippocampal AMPA receptor-dependent synaptic transmission, synaptic plasticity, and working memory. J. Neurosci. *26*, 223–232.

Chan, C.S., Levenson, J.M., Mukhopadhyay, P.S., Zong, L., Bradley, A., Sweatt, J.D., and Davis, R.L. (2007). Alpha3-integrins are required for hippocampal long-term potentiation and working memory. Learn. Mem. *14*, 606–615.

Coiro, P., Stoenica, L., Strauss, U., and Brauer, A.U. (2014). Plasticity-related gene 5 promotes spine formation in murine hippocampal neurons. J. Biol. Chem. *289*, 24956–24970.

Delwel, G.O., de Melker, A.A., Hogervorst, F., Jaspars, L.H., Fles, D.L., Kuikman, I., Lindblom, A., Paulsson, M., Timpl, R., and Sonnenberg, A. (1994). Distinct and overlapping ligand specificities of the alpha 3A beta 1 and alpha 6A beta 1 integrins: recognition of laminin isoforms. Mol. Biol. Cell *5*, 203–215.

Distler, U., Schmeisser, M.J., Pelosi, A., Reim, D., Kuharev, J., Weiczner, R., Baumgart, J., Boeckers, T.M., Nitsch, R., Vogt, J., et al. (2014). In-depth protein profiling of the postsynaptic density from mouse hippocampus using data-independent acquisition proteomics. Proteomics *14*, 2607–2613.

Ethell, I.M., and Pasquale, E.B. (2005). Molecular mechanisms of dendritic spine development and remodeling. Prog. Neurobiol. *75*, 161–205.

Fischer, M., Kaech, S., Knutti, D., and Matus, A. (1998). Rapid actin-based plasticity in dendritic spines. Neuron *20*, 847–854.

Halpain, S., Hipolito, A., and Saffer, L. (1998). Regulation of F-actin stability in dendritic spines by glutamate receptors and calcineurin. J. Neurosci. *18*, 9835–9844.

Hanke, J.H., Gardner, J.P., Dow, R.L., Changelian, P.S., Brissette, W.H., Weringer, E.J., Pollok, B.A., and Connelly, P.A. (1996). Discovery of a novel, potent, and Src family-selective tyrosine kinase inhibitor. Study of Lck- and FynT-dependent T cell activation. J. Biol. Chem. *271*, 695–701.

Huang, Z., Shimazu, K., Woo, N.H., Zang, K., Muller, U., Lu, B., and Reichardt, L.F. (2006). Distinct roles of the beta 1-class integrins at the developing and the mature hippocampal excitatory synapse. J. Neurosci. *26*, 11208–11219.

Kerrisk, M.E., Greer, C.A., and Koleske, A.J. (2013). Integrin alpha3 is required for late postnatal stability of dendrite arbors, dendritic spines and synapses, and mouse behavior. J. Neurosci. *33*, 6742–6752.

Kim, S.M., Kwon, M.S., Park, C.S., Choi, K.R., Chun, J.S., Ahn, J., and Song, W.K. (2004). Modulation of Thr phosphorylation of integrin beta1 during muscle differentiation. J. Biol. Chem. *279*, 7082–7090.

Klinghoffer, R.A., Sachsenmaier, C., Cooper, J.A., and Soriano, P. (1999). Src family kinases are required for integrin but not PDGFR signal transduction. EMBO J. *18*, 2459–2471.

Lambrecht, C., Haesen, D., Sents, W., Ivanova, E., and Janssens, V. (2013). Structure, regulation, and pharmacological modulation of PP2A phosphatases. Methods Mol. Biol. *1053*, 283–305.

Lenter, M., Uhlig, H., Hamann, A., Jeno, P., Imhof, B., and Vestweber, D. (1993). A monoclonal antibody against an activation epitope on mouse integrin chain beta 1 blocks adhesion of lymphocytes to the endothelial integrin alpha 6 beta 1. Proc. Natl. Acad. Sci. USA *90*, 9051–9055.

Luo, B.H., Carman, C.V., and Springer, T.A. (2007). Structural basis of integrin regulation and signaling. Annu. Rev. Immunol. *25*, 619–647.

McDermott, M.I., Sigal, Y.J., Crump, J.S., and Morris, A.J. (2006). Enzymatic analysis of lipid phosphate phosphatases. Methods *39*, 169–179.

McKinney, R.A., Capogna, M., Durr, R., Gahwiler, B.H., and Thompson, S.M. (1999). Miniature synaptic events maintain dendritic spines via AMPA receptor activation. Nat. Neurosci. *2*, 44–49.

Monleon, D., Esteve, V., Kovacs, H., Calvete, J.J., and Celda, B. (2005). Conformation and concerted dynamics of the integrin-binding site and the C-terminal region of echistatin revealed by homonuclear NMR. Biochem. J. *387*, 57–66.

Moolenaar, W.H., van Meeteren, L.A., and Giepmans, B.N. (2004). The ins and outs of lysophosphatidic acid signaling. Bioessays *26*, 870–881.

Ning, L., Tian, L., Smirnov, S., Vihinen, H., Llano, O., Vick, K., Davis, R.L., Rivera, C., and Gahmberg, C.G. (2013). Interactions between ICAM-5 and beta1 integrins regulate neuronal synapse formation. J. Cell Sci. *126*, 77–89.

Peeva, G.P., Angelova, S.K., Guntinas-Lichius, O., Streppel, M., Irintchev, A., Schutz, U., Popratiloff, A., Savaskan, N.E., Brauer, A.U., Alvanou, A., et al. (2006). Improved outcome of facial nerve repair in rats is associated with enhanced regenerative response of motoneurons and augmented neocortical plasticity. Eur. J. Neurosci. *24*, 2152–2162.

Perrotti, D., and Neviani, P. (2013). Protein phosphatase 2A: a target for anticancer therapy. Lancet Oncol. *14*, e229–e238.

Pradhan, S., Alrehani, N., Patel, V., Khatlani, T., and Vijayan, K.V. (2010). Cross-talk between serine/threonine protein phosphatase 2A and protein tyrosine phosphatase 1B regulates Src activation and adhesion of integrin alphaIIbbeta3 to fibrinogen. J. Biol. Chem. *285*, 29059–29068.

Sakai, T., Jove, R., Fassler, R., and Mosher, D.F. (2001). Role of the cytoplasmic tyrosines of beta 1A integrins in transformation by v-src. Proc. Natl. Acad. Sci. USA *98*, 3808–3813.

Sala, C., and Segal, M. (2014). Dendritic spines: the locus of structural and functional plasticity. Physiol. Rev. *94*, 141–188.

Savaskan, N.E., Brauer, A.U., and Nitsch, R. (2004). Molecular cloning and expression regulation of PRG-3, a new member of the plasticity-related gene family. Eur. J. Neurosci. *19*, 212–220.

Schaller, M.D. (2001). Paxillin: a focal adhesion-associated adaptor protein. Oncogene *20*, 6459–6472.

Shi, Y., and Ethell, I.M. (2006). Integrins control dendritic spine plasticity in hippocampal neurons through NMDA receptor and Ca^{2+}/calmodulin-dependent protein kinase II-mediated actin reorganization. J. Neurosci. *26*, 1813–1822.

Sigal, Y.J., McDermott, M.I., and Morris, A.J. (2005). Integral membrane lipid phosphatases/phosphotransferases: common structure and diverse functions. Biochem. J. *387*, 281–293.

Sigal, Y.J., Quintero, O.A., Cheney, R.E., and Morris, A.J. (2007). Cdc42 and ARP2/3-independent regulation of filopodia by an integral membrane lipid-phosphatase-related protein. J. Cell Sci. *120*, 340–352.

Takahashi, K., and Suzuki, K. (2006). Regulation of protein phosphatase 2A-mediated recruitment of IQGAP1 to beta1 integrin by EGF through activation of Ca^{2+}/calmodulin-dependent protein kinase II. J. Cell. Physiol. *208*, 213–219.

Takai, A., Murata, M., Torigoe, K., Isobe, M., Mieskes, G., and Yasumoto, T. (1992). Inhibitory effect of okadaic acid derivatives on protein phosphatases. A study on structure-affinity relationship. Biochem. J. *284*, 539–544.

Thompson, P.M., Tolbert, C.E., and Campbell, S.L. (2013). Vinculin and metavinculin: oligomerization and interactions with F-actin. FEBS Lett. *587*, 1220–1229.

Tokumitsu, H., Hatano, N., Tsuchiya, M., Yurimoto, S., Fujimoto, T., Ohara, N., Kobayashi, R., and Sakagami, H. (2010). Identification and characterization of PRG-1 as a neuronal calmodulin-binding protein. Biochem. J. *431*, 81–91.

Trimbuch, T., Beed, P., Vogt, J., Schuchmann, S., Maier, N., Kintscher, M., Breustedt, J., Schuelke, M., Streu, N., Kieselmann, O., et al. (2009). Synaptic PRG-1 modulates excitatory transmission via lipid phosphate-mediated signaling. Cell *138*, 1222–1235.

Unichenko, P., Kirischuk, S., Yang, J.W., Baumgart, J., Roskoden, T., Schneider, P., Sommer, A., Horta, G., Radyushkin, K., Nitsch, R., et al. (2016). Plasticity-related gene 1 affects mouse barrel cortex function via strengthening of Glutamatergic Thalamocortical transmission. Cereb. Cortex *26*, 3260–3272.

Velmans, T., Battefeld, A., Geist, B., Farres, A.S., Strauss, U., and Brauer, A.U. (2013). Plasticity-related gene 3 promotes neurite shaft protrusion. BMC Neurosci. *14*, 36.

Vogt, J., Glumm, R., Schluter, L., Schmitz, D., Rost, B.R., Streu, N., Rister, B., Bharathi, B.S., Gagiannis, D., Hildebrandt, H., et al. (2012). Homeostatic regulation of NCAM polysialylation is critical for correct synaptic targeting. Cell. Mol. Life Sci. *69*, 1179–1191.

Vogt, J., Yang, J.W., Mobascher, A., Cheng, J., Li, Y., Liu, X., Baumgart, J., Thalman, C., Kirischuk, S., Unichenko, P., et al. (2016). Molecular cause and

functional impact of altered synaptic lipid signaling due to a prg-1 gene SNP. EMBO Mol. Med. *8*, 25–38.

Wang, X.B., Bozdagi, O., Nikitczuk, J.S., Zhai, Z.W., Zhou, Q., and Huntley, G.W. (2008). Extracellular proteolysis by matrix metalloproteinase-9 drives dendritic spine enlargement and long-term potentiation coordinately. Proc. Natl. Acad. Sci. USA *105*, 19520–19525.

Wang, R., Bi, J., Ampah, K.K., Zhang, C., Li, Z., Jiao, Y., Wang, X., Ba, X., and Zeng, X. (2013). Lipid raft regulates the initial spreading of melanoma A375 cells by modulating beta1 integrin clustering. Int. J. Biochem. Cell Biol. *45*, 1679–1689.

Wennerberg, K., Lohikangas, L., Gullberg, D., Pfaff, M., Johansson, S., and Fassler, R. (1996). Beta 1 integrin-dependent and -independent polymerization of fibronectin. J. Cell Biol. *132*, 227–238.

Westphal, R.S., Anderson, K.A., Means, A.R., and Wadzinski, B.E. (1998). A signaling complex of Ca^{2+}-calmodulin-dependent protein kinase IV and protein phosphatase 2A. Science *280*, 1258–1261.

Xu, J., Xu, Z., Zhou, J.Y., Zhuang, Z., Wang, E., Boerner, J., and Wu, G.S. (2013). Regulation of the Src-PP2A interaction in tumor necrosis factor (TNF)-related apoptosis-inducing ligand (TRAIL)-induced apoptosis. J. Biol. Chem. *288*, 33263–33271.

Yang, G., Pan, F., and Gan, W.B. (2009). Stably maintained dendritic spines are associated with lifelong memories. Nature *462*, 920–924.

Ziv, N.E., and Smith, S.J. (1996). Evidence for a role of dendritic filopodia in synaptogenesis and spine formation. Neuron *17*, 91–102.

Developmental Cell, Volume *38*

Supplemental Information

PRG-1 Regulates Synaptic Plasticity via Intracellular PP2A/β1-Integrin Signaling

Xingfeng Liu, Jisen Huai, Heiko Endle, Leslie Schlüter, Wei Fan, Yunbo Li, Sebastian Richers, Hajime Yurugi, Krishnaraj Rajalingam, Haichao Ji, Hong Cheng, Benjamin Rister, Guilherme Horta, Jan Baumgart, Hendrik Berger, Gregor Laube, Ulrich Schmitt, Michael J. Schmeisser, Tobias M. Boeckers, Stefan Tenzer, Andreas Vlachos, Thomas Deller, Robert Nitsch, and Johannes Vogt

Supplemental Figure S1 to Figure 1

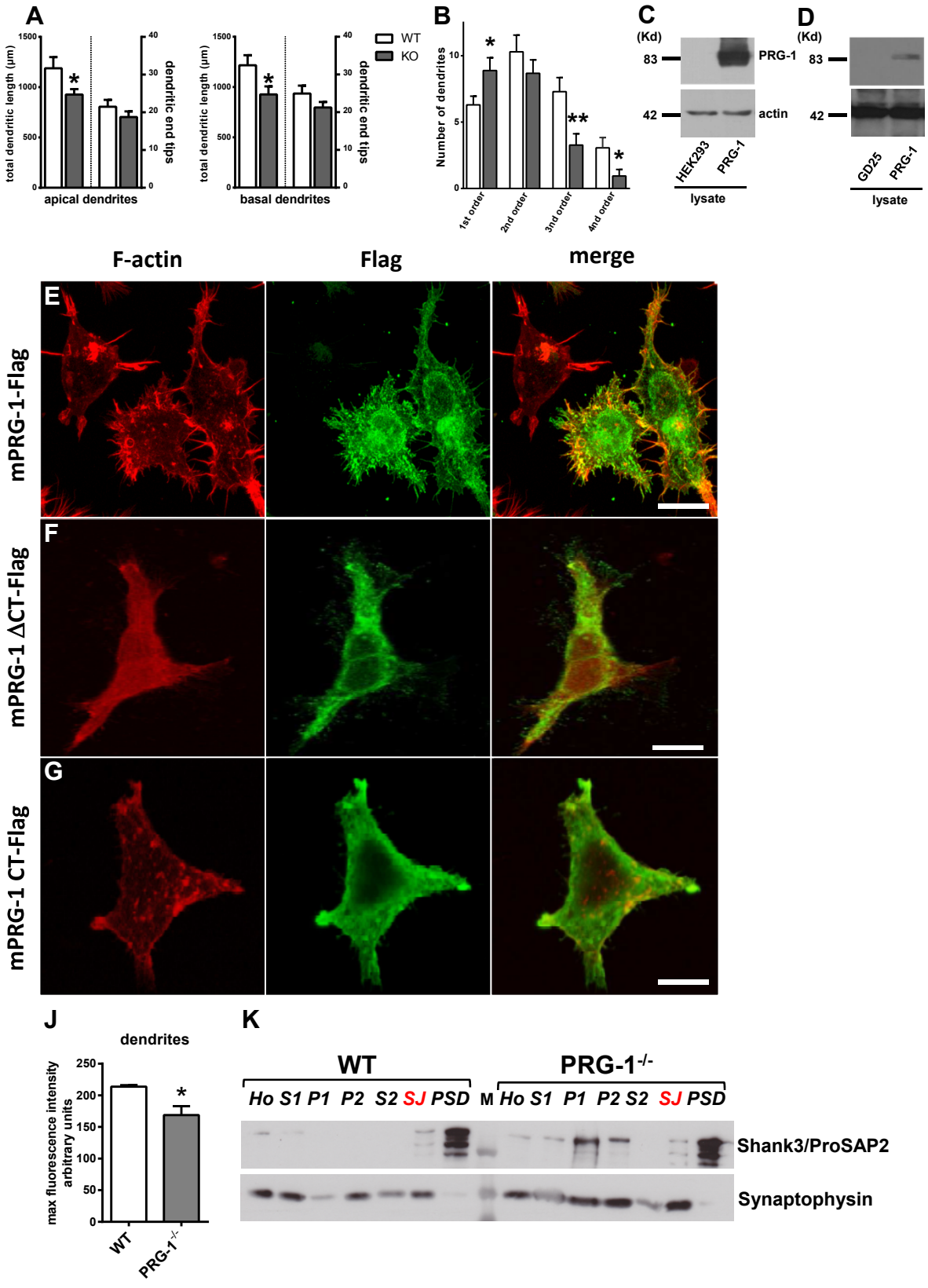

Supplemental Figure S2 to Figure 2

A

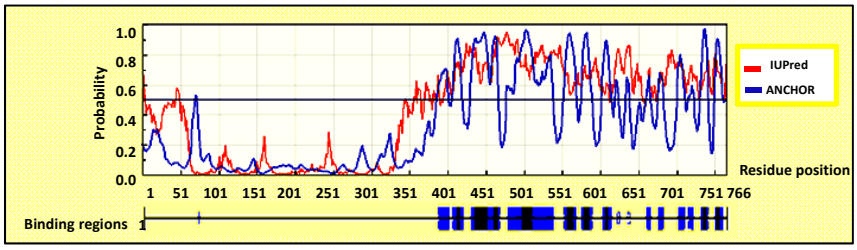

B

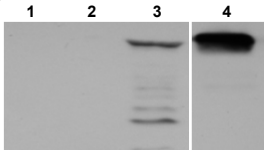

1. **HEK293 lysate**
2. **Purified HEK293**
3. **PRG1CD-TAP lysate**
4. **Purified PRG-1CD-TAP**

PRG1 interacting candidates:
PPP2R1A,
PPP2R2A,
PPP2C,
CPVL_HUMAN,
GRP75_HUMAN,
HSP7C_HUMAN,
ODO2_HUMAN, etc

C

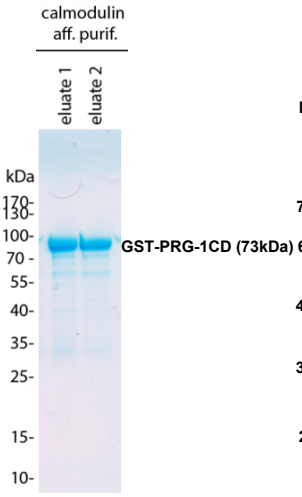

D

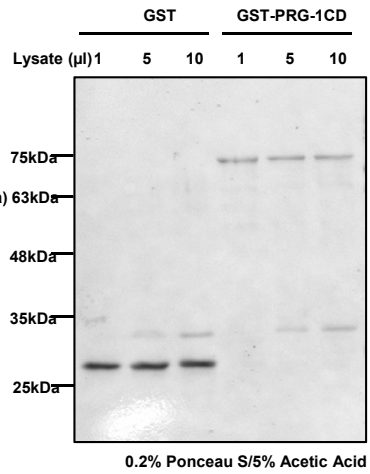

E

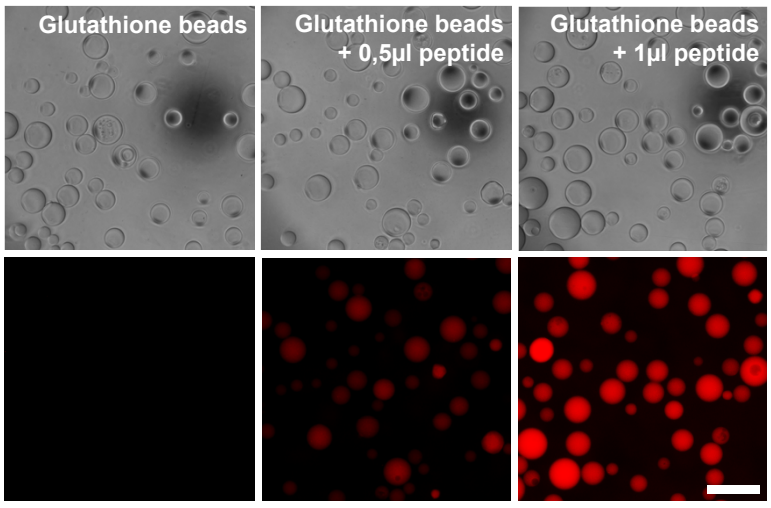

Supplemental Figure S3 to Figure 4

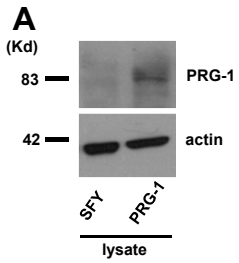

Supplemental Figure S4 to Figure 5

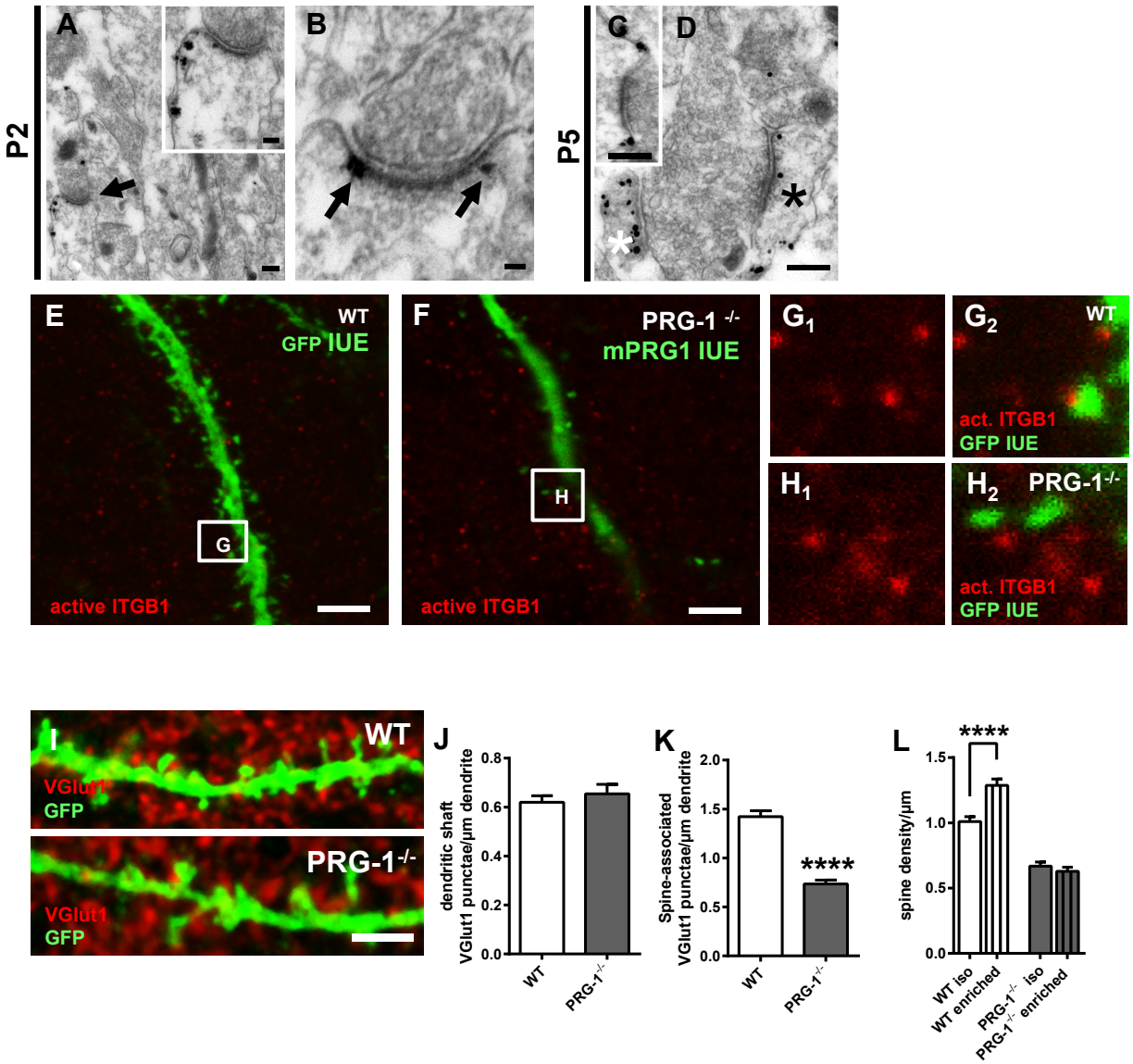

Supplemental Figure S5 to Figures 2-5

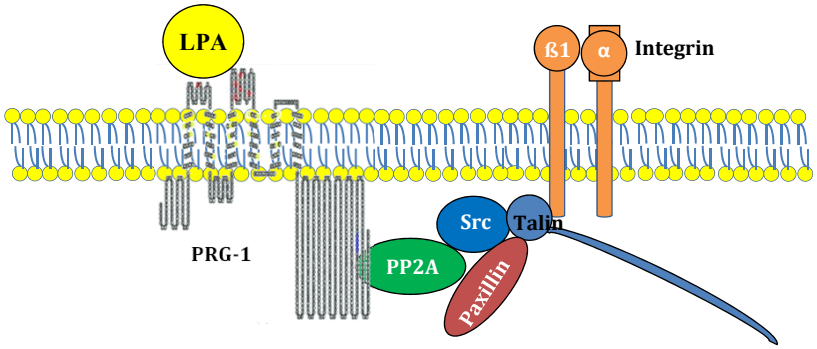

Supplemental Figure Legends

Supplemental Figure S1 related to Fig 1.

(A) Dendritic length in the apical and the basal dendrites of PRG-1$^{-/-}$ neurons is significantly reduced while and the number of dendritic end tips is not altered (n=17 WT and 19 PRG-1$^{-/-}$ neurons; Mann-Whitney test was performed for analysis of apical dendritic length and t-test were performed for all other comparisons).

(B) Dendritic arborization as assessed by comparison of number of dendritic segments of different order is significantly altered in PRG-1$^{-/-}$ neurons (n=17 WT and 19 PRG-1$^{-/-}$ neurons; t-test).

(C,D) Western blots demonstrating lack of PRG-1 in HEK-293 (C) and GD25 cells (D), and overexpression of PRG-1 in theses cell lines, respectively.

(E) HEK-293 cells display numerous actin containing filopodia upon full length PRG-1 transfection. PRG-1 is visualized via a fused Flag-tag (PRG-1-Flag fusion protein).

(F,G) HEK-293 cells expressing either a truncated PRG-1 (F), missing the intracellular C-term (mPRG-1ΔCT-Flag), or expressing only the intracellular C-term of PRG-1 (G, mPRG-1 CT-Flag), did not display filopodia. Scale bar E-G: 20 µm.

(J) Analysis of maximal fluorescence intensity of active ITGB1 signal revealed a decrease in PRG-1$^{-/-}$ neurons.

(K) Western blot of different steps of the Synaptic junction (SJ) preparation. Note the present synaptophysin (presynaptic marker) and the Shank3/ProSAP2 (postsynaptic marker; (Baron et al., 2006)) signal in the SJ fraction pointing to the presence of the presynaptic and the postsynaptic compartments in this fraction.

Supplemental Figure S2 related to Fig 2.

(A) Flexibility analysis of PRG-1 demonstrates high probability of PRG-1 cytoplasmic domain to bind with other molecules.

(B) Purification of intracellular C-terminal PRG-1 domain (PRG-1CD-TAP) according to standard procedures (Agilent technologies) and UPLC-MS analysis of the PRG1 interactome revealed novel PRG1 interacting candidates.

(C) Coomassie staining of the purified fusion construct of GST and PRG-1 C-terminal domain (GST-PRG-1CD) used for pulldown experiments. After glutathione affinity purification, GST-PRG-1CD was affinity purified using its described calmodulin interaction (Tokumitsu et al., 2010). The faint other remaining bands appear to result from degradation of the PRG-1 C-terminal domain, because they are exclusively between the sizes of the full length fusion

construct and GST alone. Furthermore GST containing fragments were detected by WB in this region (Fig. 2E).

(D) Ponceau S staining after protein transfer of pulldown product from SDS-PAGE to nitrocellulose membrane which was subsequently used for WB. After in vitro production of PPP2R2A, 1, 5 and 10 µl of the resulting lysate were used for pulldown experiment as indicated.

(E) Brightfield images (upper row) of glutathione beads incubated with different concentrations of the TAMRA-tagged PRG-1-554-588 peptide. Fluorescent images (lower row) showing the TAMRA-tagged PRG-1-554-588 peptide immobilized on glutathione beads. The different fluorescence intensities reflect the different concentrations of the peptide immobilized to glutathione beads. Control beads are devoid any fluorescence. Scale bar: 250 µm.

Supplemental Figure S3 related to Fig 4.

(A) Western Blot demonstrating lack of PRG-1 in SFY cells, and overexpression of PRG-1 in this cell line.

Supplemental Figure S4 related to Fig 5.

(A) PRG-1 expression was already found at P2, when CA1 neurons start to form first synapses. Insert shows a magnification of the stubby spine synapse shown in A.

(B) In more mature synapses found at this age, PRG-1, as shown by gold particles, is already expressed at the postsynaptic density of glutamatergic synapses and displays a similar expression pattern as revealed at adult ages.

(C,D) At P5, PRG-1 expression in CA1 neurons was observed at different stages of synapse formation: in dendritic filopodia contacting presynaptic terminals but not yet forming mature synaptic contacts (white asterisk), in stubby spines as shown in C, or in typical spines displaying PRG-1 expression at the postsynaptic density (black asterisk).

(E) Active ITGB1-staining in an in-utero *GFP* electroporated wildtype (wt) mouse displays clear punctae in the stratum radiatum (SR) of the hippocampal CA1 region.

(F) Image of in an in-utero GFP electroporated wildtype (PRG-$1^{-/-}$) mouse displays confirms lower spine density.

($G_{1,2}$) Higher magnification of the boxed area in the wt SR confirmed active ITGB1-expression at the tip of dendritic spines.

($H_{1,2}$) Higher magnification of the boxed area in the PRG-1$^{-/-}$ SR shows that active ITGB1-expression was not confined to dendritic spines.

(I) VGlut1-staining showing glutamatergic presynaptic terminals along a GFP-expressing dendritic segment (Thy-1 L21 line) in a WT and in a PRG-1$^{-/-}$ animal.

(J) Quantitative assessment of dendritic associated VGlut1-punctae revealed no difference between WT and PRG-1$^{-/-}$ animals (n=51 WT dendritic segments and 49 PRG-1$^{-/-}$ dendritic segments, unpaired t-test).

(K) Spine-associated VGlut-1 punctae revealed a significant decrease in PRG-1$^{-/-}$ mice which is in line with reduced spine densities found in these animals (n=51 WT dendritic segments and 49 PRG-1$^{-/-}$ dendritic segments, unpaired t-test).

(L) Spine density was significantly increased in WT animals kept under enriched conditions when compared to those kept in isolation. In contrast, in PRG-1$^{-/-}$ animals, dynamic regulation of spine density under enriched conditions was aborted and remained at the same low levels as observed in PRG-1$^{-/-}$ animals kept under isolation conditions.

Scale Bars: A: 200nm, insert: 80nm ;B: 40nm; C,D: 200nm; E,F: 5 µm, I: 4µm.

Supplemental Figure S5 related to Figures 2-5.

Schematic diagram of the signaling pathway analyzed.

Supplemental Experimental Procedures

Isolation, culture and analysis of hippocampal neurons

Primary hippocampal neurons from embryonic day 17 (E17) pregnant mice were prepared as previously described (Vogt et al., 2012). Briefly, after brain dissection and trypsin digestion, 10^5 neurons triturated using fire polished glass pipets were seeded on GG-18-fibronectin (neuVitro) or poly-l-lysine coated coverslips in Minimum Essential Medium (Gibco) supplemented with 10% Horse Serum, 100 U/ml penicillin and 100 µg/ml streptomycin (Gibco), 0.6% Glucose (Fresenius Kabi) and kept at 37 °C/5% CO_2. After 3 h, neurons were washed once with pre-warmed PBS, and incubated with Neurobasal Medium (Gibco) supplemented with 2% B-27, 100 units/ml penicillin, 100 µg/ml streptomycin and 0.5 mM glutamine (Gibco). For analyses, neurons were either 1. transfected at days in vitro 8 (DIV) with pEGFP-N1 or pEGFP-N1 combined with *pPRG-1-FLAG* (1:1) and analyzed at DIV14 or 2. treated with FTY720 (100 nM) starting at DIV6, transfected at DIV10 with a pCAG-IRES-EGFP vector (Kawauchi et al., 2003) and analyzed at DIV12 or 3. transfected at DIV 8, treated for 24 h with 1 nM Okadaic acid (OA) at DIV9 and analyzed at DIV10. Neurons were subsequently fixed with 4% paraformaldehyde, permeabilized, blocked with PBS containing 0.2% Triton X-100 and 5% goat serum (Vector Laboratories) and incubated with one or a combination of the following primary antibodies: mouse monoclonal anti-FLAG (M2, 1:1000, Sigma), rat monoclonal anti-active integrin ß1 (ITGB1, 9EG7, 1:200, BD Biosciences), rat anti-ITGB1 (1:200, MAB2405, R&D Systems), mouse anti-PSD95 (Synaptic Systems), rabbit anti-PRG-1 (1:2500 custom-made antibody against aa 624-637, NP_808332 as described by (Trimbuch et al., 2009)) or rabbit anti-GFP (1:1000, Abcam).

Light microscopy and Sholl analysis.

pEGFP-N1 transfected neurons were converted after fixation with diaminobenzidine (DAB) using a GFP-antibody (abcam) and a biotinylated secondary antibody (Vector Laboratories). DAB labeled neurons from WT and PRG1-KO were analysed by transmitted light microscopy. Images were taken using an upright Zeiss microscope and a 20x objective (numerical aperture 0.6). Analyses were done with the software ImageJ. By using Sholl analysis (Sholl, 1953) we could quantify the number of dendritic intersections of a neuron with cross concentric circles (from 50 µm to 350 µm diameter). Furthermore we measured total dendritic length on both apical and basal dendrites and determined the branchpoints of higher order dendrites.

Quantitative analysis of neurons

Neurons were imaged with a Leica SL or a Leica TCS SP8 confocal laser scanning microscope equipped with a white light laser (WLL) using identical laser power settings and acquisition properties for the compared conditions. Spine analysis, analysis of total and active ITGB1 expression in cell bodies and dendritic segments, respectively, were performed by an experimenter blinded to the experimental conditions using ImageJ. Mean fluorescence was quantified as grey value along dendritic segments using ImageJ. Total length of dendritic segments assessed was at least 900 µm per condition. To ensure that the analysis was not confounded by the presence of clusters of activated ITGB1 in PRG-1$^{-/-}$ neurons that contain higher amounts of active ITGB1 as in controls, clusters of active ITB1 in PRG-1$^{-/-}$ neurons were assessed in their maximal pixel grey value with those of wt neurons (Supplemental Fig. S1J).

For delineation of the corresponding ROIs using the free hand selection tool in ImageJ, images were (over-)enhanced in brightness and contrast using ImageJ, allowing for determination of dendritic segments. ROIs were then transferred to the original image and measures were performed using ImageJ. For assessment of active ITGB1 expression in PSD95 punctae on the dendritic shaft, images were thresholded using background values and ROIs were detected using the "analyse particle" function of ImageJ. To avoid for bias by unspecific recognition, only particles bigger than 0.025 µm^2 (10 pixel size) were taken into account. ROIs were then transferred to original images and mean values were measured using ImageJ. In order to compare values for different experimental conditions, all values were calculated in percent of the corresponding WT values.

Fluorescence microscopy spine and dendritic synapse quantification.

GFP positive brain slices and fluorescently labeled cell culture neurons were imaged with a Leica confocal laser-scanning microscope (SL or SP8). Single cell overview images were done with a 40x oil objective (numerical aperture 1.25). For spine measurement a 63x oil objective (numerical aperture 1.4; optical zoom 4 or zoom 5) was used for z-series stacks with a step size of 0.2µm. Fluorescent images were quantified using ImageJ. Spines were defined as dendritic protrusions from 0.5µm up to 5µm in length and were manually counted along a selected dendritic segment using ImageJ. In brain slices we focus our analyses on three populations of dendrites: (1) the dendrites within the middle molecular layer of granule cells; (2) stratum radiatum and (3) stratum oriens of pyramidal neurons of the CA1 region. Analysis of dendritic and spine synapses was performed in the CA1 region. For each genotype and age around 1000 spines or at least 1000 µm dendritic length were measured,

dependent which condition was fulfilled first. For each dendritic segment the number of spines per µm dendrite was calculated and data from one group were averaged.

Long-term potentiation (LTP)

Mice (16-18 day-old mice for data shown in Fig.1F or adult mice either untreated or treated over 30 days with 5 mg/kg FTY720 body weight/day (controls were treated in the same way using the solvent) for data shown in Fig. 3L,M, Fig. 5L) were anesthetized with isoflurane and rapidly decapitated. Experiments were performed as previously described (Fan, 2013). Transverse slices (400 µm) were prepared using a vibratome (Leica VT1200S) and immersed in ice cold artificial cerebrospinal fluid (ACSF) containing 126 mM NaCl, 2.5 mM KCl, 1.25 mM NaH_2PO_4, 1 mM $MgCl_2$, 2 mM $CaCl_2$, 26 mM $NaHCO_3$ and 10 mM D-glucose (saturated with 95% O_2 and 5% CO_2). Slices were incubated at 32 °C for at least 1 h before transfer to a submersion-type chamber for recording. Slices were allowed to recover for 30 min in the recording chamber after positioning of recording and stimulating electrodes. Field excitatory postsynaptic potentials (fEPSPs) in CA1 stratum radiatum were evoked by stimulation of Schaffer-collateral fibers with biphasic constant pulses (0.2 ms/polarity) at 0.033 Hz. fEPSPs were recorded at 30-40% of the maximum amplitude obtained in an input-output curve test. In Fig. 1F, long-term potentiation (LTP) was induced with high frequency stimulation (HFS) consisting 3 trains of 100 stimuli at 100 Hz, 10 min inter-train interval. In Fig. 3L,M and Fig 5L, LTP was induced with theta-burst stimulation (TBS): 3 trains of 10 bursts at 5 Hz, with each burst consisting 4 stimuli at 100 Hz, 30 s inter-train interval. Data were recorded every 30 sec and was averaged in 5 min bins. In order to avoid bias by outlier values, outlier analysis was performed using GraphPad Prism 6 (Version 6.07) using the ROUT method which is able to identify multiple outliers.

DNA constructs

Mouse *PRG-1* and human *ITGB1* cDNAs were amplified by One-Step RT-PCR Kit (Roche) using mRNA from mouse cortex or HEK-293 cells as template respectively. *PRG-1* coding sequence was cloned into pIRESneo3 (Clontech) between NheI and BamHI to get pIRESneo3-PRG-1; *PRG-1CD* (PRG-1 cytoplasmic C-terminal domain) coding sequence was cloned into pNTAPB (Stratagene) between BamHI and ApaI restriction sites to get pNTAPB-PRG-1CD; Human *ITGB1* coding sequence was cloned into pIRESpuro3 (Clontech) between NheI and BamHI to get pIRESpuro3-hITGB1. Truncated form of *PRG1* coding for amino acids 554 to 588 (CaM binding domain), was prepared by using QuickChangeII XL Site-Directed Mutagenesis Kit (Stratagene) using pIRESneo3-PRG1 as

template plasmid. *Src* cDNA was from Addgene and subcloned into pIREShyg3 between NheI and BamHI. The plasmids pCAG-mPRG-1 and pCAG-cre were constructed by inserting the corresponding coding frame into the multiple cloning site (MCS) of a pCAG-IRES-eGFP vector (Kawauchi et al., 2003). pPRG1-FLAG was prepared using pEGFP-N1 (Stratagene) as backbone, its EGFP coding sequence was replaced by FLAG sequence from p3xFLAG-CMV (Sigma) and PRG-1 reading frame or its mutated forms were inserted between EcoRI and BamHI. R345T mutant of PRG-1 (*PRG-1*^{R345T}) was constructed as described (Vogt et al., 2016). Insertion of DNA coding the C-terminal cytoplasmic domain of murine *PRG-1* (amino acids 338-766) into the vector pGEX-6P-1 (GE Healthcare) between the BamHI and NotI restriction sites using standard cloning techniques resulted the plasmid for bacterial production of a GST-PRG-1CD fusion protein.

Cell culture, transfection, cell line establishment and immunocytochemistry

HEK-293, GD25 (provided by Reinhard Faessler) and MEF-SFY (provided by Mirko Schmidt) cell lines were cultured in DMEM (Gibco) supplemented with 10% fetal bovine serum (Pan-Biotech), 100 U/ml penicillin, 100 µg/ml streptomycin, 2 mM L-glutamine and 0.1 mM MEM non-essential amino acids (all from Gibco) at 37 °C / 5% CO_2. Stable cell lines were established by continual application of G418 (600 µg/ml), hygromycin (50 µg/ml) or puromycin (0.5 µg/ml) in complete DMEM after calcium phosphate or lipofectamine 2000 (invitrogen) transfection, and followed by picking and amplifying antibiotics resistant clones according to standard protocol. The selected and amplified cell clones were maintained in complete DMEM containing corresponding antibiotics at half the concentrations for selection. Introduction of DNA for transient expression of exogenous genes was carried out using classical calcium phosphate or lipofectamine (ThermoFisher Scientific) methods on HEK-293 and GD25 cells. For immunostaining, cells were fixed with 4% paraformaldehyde, permeabilized, blocked with PBS containing 0.2% Triton X-100 and 5% goat serum (Vector Laboratories) or 10% FCS and incubated mouse monoclonal anti-Vinculin (SPM227, 1:200, abcam), mouse monoclonal anti-FLAG (M2, 1:1000, Sigma), Phalloidin (Sigma) and subsequently visualized with a secondary goat anti mouse antibody conjugated to Alexa Fluor 546 or to Alexa Fluor 488 (1:1000, Invitrogen). Confocal imaging was performed as described above.

Cell adhesion assay

Cell adhesion was assayed as described in instruction manual of ECM Cell Adhesion Array Kit (Chemicon) with little modification. Briefly, cells at log phase were starved for 24h, then detached from the dishes using 2 mM EDTA in DPBS-CMF (Dulbecco's phosphate-buffered

saline without calcium and magnesium, Gibco) and collected. Single cell suspensions were prepared in HBSS-CMF (Hanks buffered salts solution without calcium and magnesium) supplemented with 0.1**%** fatty acid free BSA (Albumin bovine fraction V) (SERVA) and 25 mM HEPES to achieve 1.0 x 10^6 cells/ml, 100 µl cells (1x 10^5 cells) were seeded in each well of the ECM array plate or fibronectin or laminin coated strips (Chemicon) having been rehydrated with DPBS-CMF for 10 min at room temperature. After 2 h incubation at 37 °C and 5% CO_2, non-adherent cells were removed by washing 3 times with DPBS-CMF, whereas 100 µl of Cell Stain Solution (Chemicon) per well were added to the remaining adherent cells and incubated for 5 min at room temperature. After staining the wells were washed 3 to 5 times with deionized water and then air dried. Random fields from each well were taken for images (10x magnification) and the number of adherent cells was counted, or the cell-bound stain was solubilized by 100 µl Extraction Buffer (Chemicon) and measured at 540-570 nm on a microplate reader. For cell adhesion inhibition assays cells were preincubated with the following drugs respectively: 100 nM Echistatin (Sigma) for 1 h, 2 µg/ml anti-ITGB1 (P5D2, abcam), 1 µM LPA (Enzo Life Sciences) added just before adherent, 1 µg/ml FTY720 (Sigma) for 1 h, 100 nM Okadaic acid (Biomol) for 2 h, 1 µM PP2 (Sigma) for 1 h, 5 mM Methyl-ß-cyclodextrin (MßCD), 25 µg/ml Nystatin (Sigma) for 30 min.

Flow cytometry

All flow cytometry analyses were carried out on a FACS Canto II cytometer (BD Biosciences). To analyze ITGB1 activation, HEK-293 cell lines expressing PRG-1 and HEK-293 cells were cultured till around 80% confluent, washed twice with DMEM without phenol red indicator to get rid of dead cells, harvested, resuspended in DMEM and filtered through cell strainer for further use. One million cells were preincubated at 4 °C for 10 min with 5 µg human IgG (Sigma) to block Fc receptors, then incubated with 5 µg FITC-conjugated ITGB1 antibody (TDM29/CBL481, Millipore) for total surface ITGB1 staining or antibody to activated ITGB1 (HUTS-4, Millipore) followed by Alexa 488-conjugated F(ab´)2 fragment of rabbit anti-mouse IgG (1:2000, Invitrogen) staining. Integrin activation status was also analyzed by its echistatin affinity. For this aim, one million cells were firstly incubated with 100 nM echistatin (sigma), then incubated with 5 µg rabbit anti-echistatin antibody (Millipore) and subsequently with Alexa 488-conjugated F(ab´)2 fragment of goat anti-rabbit IgG (1:2000, Invitrogen). For intracellular talin staining, one million prepared single cell suspension was fixed with ice cold methanol and permeabilized by 0.1% Triton X-100, then incubated with talin rod domain (8D4), talin pS425 (ECM Bioscience) or talin head domain (TA205, Sigma), followed by Alexa 488-conjugated F(ab´)2 fragment of rabbit anti-mouse or goat anti-rabbit IgG (1:2000, Invitrogen).

Synaptic junction (SJ) preparation

SJ fraction was isolated as recently described (Distler et al., 2014). The animal experiments were conducted in accordance with national laws and approved by the local authorities. Subcellular fractionation was performed from six independent samples. Each sample contained hippocampi pooled from 10-11 mice. All buffers were supplemented with protease and phosphatase inhibitor mix (Roche) and all steps were either performed at 4 °C or on ice. Briefly, tissue was homogenized in buffer (320 mM sucrose, 5 mM HEPES, pH 7.4) using a teflon douncer. The homogenate (Ho) was centrifuged for 10 min at 1,000 x g to remove cell debris and nuclei (P1). The supernatant (S1) was further centrifuged for 20 min at 12,000 x g to obtain the soluble fraction (S2) and the crude synaptosomes (P2). P2 was resuspended in a Tris buffer (320 mM sucrose, 5 mM Tris/HCl, pH 8.1) and centrifuged in a sucrose density gradient (0.8 M/1.0 M/1.2 M) for 2 h at 200,000 x g. Purified synaptosomes were collected from the 1.0/1.2 interphase, diluted in five volumes of 1 mM Tris/HCl, pH 8.1, lysed for 30 min by stirring and centrifuged for another 30 min at 33,000 x g. The resulting pellet was resuspended in 5 mM Tris/HCl, pH 8.1, and centrifuged in another sucrose density gradient (0.8 M/1.0 M/1.2 M) for 2 h at 200,000 x g for additional purification. Synaptic junctions (SJ) were collected from the 1.0/1.2 interphase, subsequently resuspended in Tris buffer containing 0.5% Triton X-100, stirred for 15 min and centrifuged for another 30 min at 33,000 x g to obtain a one-Triton extracted PSD fraction (PSD). For characterization of the PSD-preparation an antibody against Shank3 (described in (Schmeisser et al., 2012)) and an antibody against Synaptophysin (Abcam) were used.

Western Blotting (WB)

WB was performed according to standard procedures. Briefly, samples were separated by SDS-PAGE using 10% polyacrylamide gels, and blotted on a nitrocellulose membrane (0.45 µm; BIO-RAD, USA) by semi-dry transfer cell (BIO-RAD, USA) at 100 mA for 40 min. Blots were blocked overnight at 4 °C in 10% non-fat dry milk, washed twice, and incubated at room temperature (RT) for 3 h with corresponding antibodies in 1% non-fat BSA. After three washes, membranes were incubated with a corresponding horseradish peroxidase-conjugated antibody (1:5000 dilution; dianova, Germany) in 1% non-fat BSA at RT for 1 h. Immunoreactive bands were detected using SuperSignal West Femto Maximum Sensitivity Substrate kit (Thermo Scientific, USA) according to standard protocols. Quantification of immunosignals was performed using ImageJ.

Preparation of the PRG-1CD interactome

Cell lines expressing PRG-1CD fusion protein with tandem streptavidin binding peptide (SBP) and calmodulin binding peptide (CBP) tags at N terminus were established as above and pull-down assays were carried out according to instruction manual of InterPlay® Mammalian TAP System (Agilent technologies). Tandem affinity purification (TAP) pulldown and control eluates were lyophilized and resolubilized in lysis buffer (7M Urea, 2M ThioUrea, 2% Chaps). Subsequently, proteins were digested using a modified filter-aided sample preparation (FASP, (Wisniewski et al., 2009)). Briefly, redissolved protein was loaded on the filter, and detergents were removed by washing three times with buffer containing 8 M urea. The proteins were then reduced using DTT, alkylated using iodoacetamide, and the excess reagent was quenched by addition of additional DTT and washed through the filters. Buffer was exchanged by washing with 50 mM NH_4HCO_3 and proteins digested overnight by trypsin (Trypsin Gold, Promega) with an enzyme to protein ratio of 1:50. After overnight digestion, peptides were recovered by centrifugation and two additional washes using 50 mM NH_4HCO_3. Flowthroughs were combined, lyophilized and redissolved in 20 µl 0.1% formic acid by sonification. The resulting tryptic digest solutions were diluted with aqueous 0.1% v/v formic acid to a concentration of 200 ng/µl and spiked with 25 fmol/µl of enolase 1 (*Saccharomyces cerevisiae*) tryptic digest standard (Waters Corporation).

UPLC-MS configuration

Nanoscale LC separation of tryptic peptides was performed with a nanoAcquity system (Waters Corporation) equipped with a HSS-T3 C18 1.8 µm, 75 µm x 250 mm analytical reversed-phase column (Waters Corporation) in direct injection mode as described before (Tenzer et al., 2011)). 0.2 µl of sample (40 ng of total protein) was injected per technical replicate. Mobile phase A was water containing 0.1% v/v formic acid, while mobile phase B was ACN containing 0.1% v/v formic acid. Peptides were separated with a gradient of 3–40% mobile phase B over 120 min at a flow rate of 300 nl/min, followed by a 10-min column rinse with 90% of mobile phase B. The columns were re-equilibrated at initial conditions for 15 min. The analytical column temperature was maintained at 55 °C. The lock mass compound, [Glu^1]-Fibrinopeptide B (100 fmol/µL), was delivered by the auxiliary pump of the LC system at 300 nl/min to the reference sprayer of the NanoLockSpray source of the mass spectrometer. Mass spectrometric analysis of tryptic peptides was performed using a Synapt G2-S mass spectrometer (Waters Corporation, Manchester, UK). For all measurements, the mass spectrometer was operated in v-mode with a typical resolution of at least 25 000 FWHM (full width half maximum). All analyses were performed in positive mode ESI. The time of flight analyzer of the mass spectrometer was externally calibrated with a NaI mixture

from **m/z** 50 to 1990. The data were post-acquisition lock mass corrected using the doubly charged monoisotopic ion of [Glu[1]]-Fibrinopeptide B. The reference sprayer was sampled with a frequency of 30 s. Accurate mass LC-MS data were collected in data-independent modes of analysis (Geromanos et al., 2009) (Silva et al., 2005) in combination with on-line ion mobility separations. For ion mobility separation, a wave height of 40 V was applied. Traveling wave velocity was ramped from 800 m/s to 500 m/s over the full IMS cycle. The spectral acquisition time in each mode was 0.7 s with a 0.05 s interscan delay. In low energy MS mode, data were collected at constant collision energy of 4 eV. In elevated energy MS mode, the collision energy was ramped from 25 to 55 eV during each 0.7 s integration. One cycle of low and elevated energy data was acquired every 1.5 s. The radio frequency (RF) amplitude applied to the quadrupole mass analyzer was adjusted such that ions from **m/z** 350 to 2000 were efficiently transmitted, ensuring that any ions observed in the LC-MS data less than **m/z** 350 were known to arise from dissociations in the collision cell. All samples were analyzed in triplicate.

UPLC-MS data processing, protein identification and statistical analysis

Continuum LC-MS data were processed and searched using ProteinLynx GlobalSERVER version 2.5.2 (Waters Corporation). The resulting peptide and protein identifications were evaluated by the software using statistical models as described (Tenzer et al., 2011). Protein identifications were assigned by searching the mouse taxon of the *UniProtKB/SwissProt* database (release 2012_01) supplemented with known possible contaminants and standard proteins (porcine trypsin, yeast enolase, BirA, streptavidin) using the precursor and fragmentation data afforded by the LC-MS acquisition method as reported (Tenzer et al., 2011). The search parameter values for each precursor and associated fragment ions were automatically set by the software using the measured mass error obtained from processing the raw continuum data. Peptide identifications were restricted to tryptic peptides with no more than one missed cleavage. Carbamidomethyl cysteine was set as fixed modification, and oxidized methionine, protein N-acetylation, and deamidation of asparagine and glutamine were searched as variable modifications. Database search was performed allowing a maximal mass deviation of 3 ppm for precursor ions and 10 ppm for fragment ions. For valid protein identification, the following criteria had to be met: at least 2 peptides were detected with together at least 7 fragments. All reported peptide identifications provided by the IDENTITY^{E}-algorithm are correct with >95% probability as described (Tenzer et al., 2011). The initial false positive rate for protein identification was set to 3% based on search of a 5x randomized database, which was generated automatically using PLGS2.5.2 by randomizing the sequence of each entry. By using replication rate of identification as a filter,

the false positive rate is further reduced to <0.1%. Additional data processing including retention time alignment, normalization, isoform/homology and replicate filtering, as well as final TOP3 based label-free quantification was performed using the ISOQuant software pipeline as described previously (Patzig et al., 2011).

Bioinformatics and statistical analysis. Hierarchal clustering analysis was performed based on absolute label-free protein quantification results provided by ISOQuant using dedicated *R* scripts in *R2.14.0* execution environment (Tenzer et al., 2011).

Immunoprecipitation and immunoblotting

HEK-293 cells expressing PRG-1 or mechanically homogenized cortex tissue were lysed in appropriate volume of lysis buffer (50 mM Tris-HCl pH 7.4, 1% Triton X-100, 1% n-Octyl ß-D-glucopyranoside, 0.1% SDS, 1 mM EDTA pH7.0, 150 mM NaCl) containing protease inhibitors (Roche) for 1 h on ice, and cleared by centrifugation for 10 min at 15000 g at 4 °C. The following lysate preclearing with agarose slurry, incubation with PRG-1 antibody (1:100), or normal rabbit IgG (1:100, Millipore) as control, and pull-down by Protein G agarose resin (Thermo Scientific) were carried out according to standard protocols. The following primary antibodies was used for immunoblotting: PRG-1 (1:3000, custom-made antibody against aa 624-637, NP_808332) (Trimbuch et al., 2009). Following antibodies were used for immunoblotting: ITGB1, PPP2R1A (81G5), PPP2R2A (100C1), PPP2C (52F8), Src (32G6), Talin (C45F1), Paxillin pY118 (1:1000) all from Cell Signaling, Caveolin-1 (Cav1) (1:2000, Sigma), PPP2C pY307 (E155, 1:1000, abcam), ß-actin (1:5000, MP Biomedicals). For immunoblotting, cell lysates or immunoprecipitated samples were separated by SDS-PAGE and transferred onto nitrocellulose membrane (Bio-Rad). After incubation with first antibodies and HRPO-conjugated secondary antibodies (1:5000, dianova), membranes were developed by ECL (Amersham Biosciences) according to standard protocols.

Proximity Ligation Assay (PLA)

The following primary antibodies were used for PLA: PRG-1 (1:1000, custom-made antibody against aa 624-637, NP_808332) (Trimbuch et al., 2009)), PPP2R2A (2G9), Src (32G6), Paxillin (1:100), Cav1 (D46G3), HA-Tag (6E2,1:200) and FAK (1:200) all from Cell Signaling, PPP2C (1D6, 1:100), ITGB1 C terminus (EP1041Y, 1:250) from Millipore, PPP2R1A (4E6) and Talin (TA205) (1:100) from Sigma, FAK central region (M246, 1:200) from ECM Bioscience and Caveolin1 (7C8, 1:125) from Thermo Scientific. The in situ PLA was used to detect protein-protein interactions in fixed cells. PRG-1 expressing or HEK-293 cells or primary neurons were fixed with 4% PFA followed by blocking with blocking solution. Then

incubations with primary antibodies, with the PLA probes (anti-mouse and anti-rabbit IgG antibodies conjugated with oligonucleotides), ligation and amplification according to the user manual of Duolink® II Fluorescence (Olink® Bioscience). Imaging was performed on a Leica SP8 confocal laser scanning microscope. For the evaluation of the specific number of dots per cell, pictures of cells with positive PLA signal were used. Cell delineation was performed by adjusting the DAPI-signal. Quantitative analysis was performed either by counting PLA-positive dots per cell/cell in the visual field or by assessment of the fluorescence signal per cell as mean gray values using ImageJ.

Purification of GST-PRG-1CD

E. coli T7Express (NEB) cells transformed with pGEX-6P-1-GST-PRG-1CD grew over night on an LB-ampicillin agar plate at 37 °C. A single colony served for inoculation of a 100 mL LB-ampicillin overnight shaking culture at 37 °C. The next day 1 L 2xYT-ampicillin medium in a 2 L shaking flask was inoculated to an OD600 of 0.1 and incubated shaking at 37 °C till the OD600 reached 0.3 at which time the cooling to 30 °C started. At an OD600 of 0.6-0.8 addition of 0.2 mM IPTG induced protein production. Cells were harvested after 4 h, weighed, suspended in an equivalent amount of 20 mM HEPES buffer pH 7.5 and frozen in liquid nitrogen. For cell disruption 12 g frozen suspended cell pellet melted in a total final volume of 30 mL lysis buffer (50 mM HEPES pH 7.5, 2 mM $MgCl_2$, 1 g/L lysozyme, EDTA free protease inhibitor (Roche)). Afterwards stirring continued for 30 min at 4 °C. All following steps were performed on ice or at 4 °C. Six cycles of 30 s ultra-sonication (Branson Sonifier 250, duty cycle 70%, output 8) followed by 30 s cooling on ice disrupted the cells. 20 min centrifugation at 14000 rpm pelleted cell debris. The clarified supernatant was adjusted to 150 mM NaCl, filtered (0.45 µm) and batch loaded for 1 h on 1 mL glutathione superflow agarose resin (Pierce) equilibrated in wash buffer (20 mM HEPES pH 7.5, 150 mM NaCl). The settled loaded resin was transferred in a gravity flow column, washed with 12 mL washing buffer and the protein was eluted with 6 mL elution buffer (20 mM Tris pH 8, 150 mM NaCl, 10 mM reduced glutathione). The eluate was adjusted to 40 mM HEPES pH 7.5, 300 mM NaCl, 5 mM $CaCl_2$, 1 mM $MgCl_2$ and supplemented with 1x EDTA-free protease inhibitor in a final volume of 7 mL. To purifiy the GST-PRG-1CD via the native calmodulin binding of the PRG-1 domain the solution was batch loaded for 1 h on 0.5 mL calmodulin sepharose 4B resin (GE Healthcare) equilibrated in washing buffer (40mM HEPES pH 7.5, 2 mM $CaCl_2$, 300 mM NaCl, 1 mM imidazole). After washing the resin with 8 mL washing buffer the protein was eluted with elution buffer (40 mM HEPES pH 7.5, 2 mM EGTA, 300 mM NaCl). The first two 1 mL fractions containing most of the purified GST-PRG-1CD were pooled.

Pulldown with purified intracellular C-terminal domain PRG-1 (GST-PRG-1CD) in a cell-free system

The regulatory subunit PP2A beta subunit PPP2R2A was produced in a cell free – rabbit reticulolysate system (Promega, L1170) following manufacturer's instructions using a pCAG-*PPP2R2A* expressing construct as a template. In this approach, rabbit reticular lysates are treated with micrococcal nuclease destroying endogenous mRNA and thus preventing background translation. Due to its cell-free nature devoid of cellular membrane components, content of membrane proteins is reduced by large. The lysate from this PPP2R2A-producing system excludes, for the most part, putative intermediate interaction partners of PRG-1 which might mediate an indirect interaction with PP2A. For in-vitro interaction studies, 1 to 10 µl of lysate were mixed with 2 µg of GST (control) or GST coupled purified PRG-1CD protein, and 10 µl of glutathione-sepharose (GE healthcare) in 200 µl of binding buffer (25 mM Tris-HCl pH 7.2, 150 mM NaCl, 1% NP-40, 5 mM $MgCl_2$, and 5% glycerol). For specific interaction studies, 0.5 µl and 1 µl of a 1 mM peptide solution corresponding to PRG-1 aa 554-588 which was tagged to TAMRA as a fluorescence indicator dye was immobilized to 10 µl of glutathione-sepharose in 200 µl binding buffer. Subsequently 200 µl of binding buffer containing 1 µl of reticular lysate was added to the resin. Binding of PRG-1 aa 554-588 to glutathione-sepharose was determined by its fluorescence TAMRA tag. Control beads showed no fluorescence signal (Supplemental Fig. S2E). Fluorescent pictures were taken on an inverse microscope from DMi8 from Leica. All pictures were taken using same settings and were adjusted for brightness and contrast in the same way. After 2 h of incubation at 4 ˚C, the resin was washed twice with ice cold binding buffer. The samples were used for 10% acrylamide gel SDS-PAGE followed by western blotting analysis on nitrocellulose membrane. PPP2R2A was detected on the membrane after blocking with 3% BSA/TBST (20mM Tris-HCl pH 7.5, 150 mM NaCl, and 0.05% Tween-20) by an anti-PP2A beta subunit antibody (Cell Signaling, 100C1 #2290) and a HRP conjugated anti-rabbit antibody (NOVEX, A16096). GST coupled protein was detected by anti-GST antibody (Santa Cruz, SC-138) and HRP conjugated anti-mouse IgG (GE healthcare, NA9310-1ML).

Lipid raft preparation

Lipid rafts were extracted according to instruction manual of Caveolae/Rafts Isolation Kit (Sigma). Briefly, for each density gradient one 10 cm dish of cells (80% confluent) were lysed with 1 ml lysis buffer containing 1% Triton X-100, OptiPrep density gradient was prepared and centrifuged at 200,000 g using SW 40 Ti rotor (Beckman) for 4 h at 4 °C. From top to bottom of the ultracentrifuge 1 ml fractions were carefully collected and transferred to a marked microcentrifuge tube.

Serine/Threonine Phosphatase Assay

For serine/threonine phosphatase assay, the elute samples were prepared according to instruction manual of InterPlay® Mammalian TAP System (Agilent technologies) from pNTAPB-PRG-1CD transfected cells and HEK-293 cells as control. Additionally, we also tested phosphatase activity in lysates. For this aim pNTAPB-PRG-1CD transfected and control cells were firstly lysed in appropriate volume of lysis buffer, freeze-thaw cycles for 3 times and cleared by centrifuge for 10 min at 15000 g at 4 °C. Then the free phosphates were removed from samples by Sephadex® G-25 resin before phosphatase assay was carried out following instructions of Serine/Threonine Phosphatase Assay System (Promega).

Transgenic animals and breeding.

Constitutive and conditional PRG-1-KO mice were used. For generation of the mice and genotyping see Trimbuch et al. (2009). To visualize the neurons, particularly the dendrites and the dendritc spines, PRG-$1^{+/-}$ animals of the constitutive mouse line were bred with Thy-1.2-EGFP_L21 mice (Caroni, 1997). To generate a PRG-$1^{-/-}$/LPA$2^{-/-}$ mouse line, heterozygous constitutive PRG-$1^{-/-}$ mice were bred with LPA2-$R^{-/-}$ mice, provided by J. Chun (Contos et al., 2002).

Electron Microscopy. For ultrastructural analysis, immunogold pre-embedding labeling was performed as described previously ((Lujan et al., 1997) (Krauss et al., 2007)). Briefly, brains were perfused with 4% paraformaldehyde, 0.05% glutaraldehyde and 15% (v/v) saturated picric acid made up in 0.1 M phosphate buffer (PB, pH 7.4), and cut with a vibratome. Free-floating sections were incubated in 10% normal donkey serum (NDS) diluted in Tris buffered saline (TBS) for 1 h at room temperature. Sections were then incubated for 36 h with the primary antibody at a dilution determined by light microscopy (see above) in TBS containing 1% NDS. After several washes in TBS, sections were incubated overnight with the secondary 1.4 nm gold coupled antibody (Nanoprobes Inc., Stony Brook, NY) raised in goat, followed by silver enhancement of the gold particles with a HQ Silver kit (Nanoprobes Inc., Stony Brook, NY). Following immunogold visualization, sections were transferred to 0.1 M PB, postfixed for 30 min with 1% osmium tetroxide in 0.1 M PB, and washed several times in PB. Finally, sections were dehydrated in a graded series of ethanol for 10 min each including block staining with 2% uranyl acetate (Serva, Heidelberg, Germany) in 70% ethanol, and flat embedded in Araldite CY212 (Serva). Thin silver sections were contrasted with uranyl

acetate and lead citrate and analyzed with a LEO 912 electron microscope equipped with a slow scan digital camera (Proscan 1K) microscope.

In-vivo experiments

All experimental procedures described below were carried out in accordance with the European Communities Council Directive regarding care and use of animals for experimental procedures and were approved by Landesuntersuchungsamt Koblenz, Germany.

In utero Electroporation and expression plasmids for IUE. The in utero electroporation experiments were carried out as described (Prozorovski et al., 2008; Trimbuch et al., 2009), 2009), in accordance with a protocol approved by the local animal welfare committee. Using in utero electroporation, PRG-1 could be deleted in conditional or re-expressed in constitutive PRG-1 KO mice in a subset of cells. For in utero electroporation plasmids were prepared at 4 µg/µl by using the EndoFree Plasmid Kit (Qiagen). Timed-pregnant mice at E15-E16 (post coitum) were anesthetized with a Ketamin-Xylazinmix (Ketamine 10mg/ml; Xylazine 1mg/ml). The uterine horns were exposed and two of the pubs were randomly chosen for injecting plasmids. The DNA solution (1-1.5 µl/embryo) was injected through the uterine wall into the lateral ventricle by pulled glass capillaries (World Precision Instruments, Sarasota, USA). Electric pulses were delivered to embryos by holding the injected brain through the uterine wall with forcep-type electrodes (CUY650P5) connected to a square–pulse generator (CUY 21 Edit, Unique Medical Imada, Miyagi, Japan). Five (5) 38-V pulses of 50 ms were applied at 950 ms intervals. The uterine horns were carefully put back into the abdominal cavity before the muscle wall and skin were stitched.

The plasmids pCAG-mPRG1 and pCAG-Cre were constructed by cloning the corresponding coding frame into the MCS of a pCAG-IRES-EGFP vector (Kawauchi et al., 2003). The pCAG–PRG1R346T vector was constructed as described (Vogt et al., 2016). For in utero electroporation 16 plasmids were prepared at 4 µg/µl by using the EndoFree Plasmid Kit (Qiagen). Timepregnant mice at E15-E16 (post coitum) were anesthetized with a Ketamin-Xylazinmix (Ketamine 10mg/ml; Xylazine 1 mg/ml). The uterine horns were exposed and two of the pubs were randomly chosen for injecting plasmids. The DNA solution (1-1.5 µl/embryo) was injected through the uterine wall into the lateral ventricle by pulled glass capillaries (World Precision Instruments, Sarasota, USA). Electric pulses were delivered to embryos by holding the injected brain through the uterine wall with forceps-type electrodes (CUY650P5) connected to a square–pulse generator (CUY 21 Edit, Unique Medical Imada, Miyagi, Japan). Five (5) 38-V pulses of 50 ms were applied at 950 ms intervals. The uterine horns

were carefully put back into the abdominal cavity before the muscle wall and skin were stitched.

Morphological analyses in WT, PRG-1$^{+/-}$ and PRG-1$^{-/-}$ animals.

For dendritic spine analysis in vivo Thy-1.2-EGFP_L21 mice were mated with PRG-1+/- mice. EGFP positive brains from WT, PRG-1$^{+/-}$ and PRG-1$^{-/-}$ were than used at the postnatal (P) ages P12, P19 and adult (>6 weeks; 3 animals per genotype and age). The first 24 h after birth were defined as P0. All mice were anesthetized (0.5% ketamin i.p.) and transcardially perfused with tyrode followed by 4% (w/v) paraformaldehyd (PFA) in 0.1 M phosphate buffer (PB). Brains were removed, postfixed overnight and sectioned horizontally with a vibratome at 50 µm thickness. For immunofluorescence stainings, brain slices were permeabilized with 0.2 % Triton, blocked with 10% normal goat serum and incubated with anti VGlut-1 antibody (1:2000, Synaptic Systems) or active ITGB1 (1:200, R&D Systems) over night. Subsequently, brain slices were washed and incubated with a secondary goat anti mouse Alexa 568 antibody. Hippocampal sections were mounted on glass slides and embedded with Prolong Gold. Animals with successfully electroporated brains were processed equally in the third week of life.

Morris Water Maze

For MWM, male age matched mice were tested from 3 month onward. All experimental procedures were carried out in accordance with the European Communities Council Directive regarding care and use of animals for experimental procedures and were approved by Landesuntersuchungsamt Koblenz, Germany.

Spatial learning and memory were tested by the Morris water maze hidden platform task using the same maze and protocol as described (Postina et al., 2004). Briefly, the platform was positioned in the same quadrant for days 1 to four and the animals were released from four different positions at the pool perimeter. Mice performed four trials per day on four consecutive days with a maximal observation length of 90 s and an inter-trial interval of 90 s. If mice did not find the platform within the given time, they were gently guided to the platform. Mice were allowed to stay on the platform for 10 s. On the fifth water maze day, after removing the platform, a probe trial (60 s) was performed. Mice were automatically monitored using a computerized video system registering moving-path and duration in defined test compartments. The hardware consisted of an IBM-type AT computer combined with a video digitizer and a CCD video camera. The software used for data acquisition and analysis was EthoVision XT® release 8.0 (Noldus Information Technology, Utrecht, Netherlands).

Learning was assessed by measuring the latency to find the platform. General activity was assessed by swim speed, where mice displayed no significant differences (data not shown) and memory capabilities, which were characterized by the time mice spent searching for the platform in each quadrant.

Analysis of spine dynamics

To analyze for dynamic changes in spine density as observed by others under enriched conditions (Rampon et al., 2000), mice (EGFP-expressing (Thy1-L21) WT and PRG-1$^{-/-}$ mice) were separated after weaning in two groups. While one group was housed in large cages with three floors which were equipped with running wheels and small houses, and where fresh food and water was offered in different places to encourage for exploratory behavior, the other group was kept in isolation in a dark environment. Spine density of first order apical dendrites in the stratum radiatum (SR) of GFP-expressing CA1-neurons was analyzed at 9 weeks of age.

Supplemental References

Baron, M.K., Boeckers, T.M., Vaida, B., Faham, S., Gingery, M., Sawaya, M.R., Salyer, D., Gundelfinger, E.D., and Bowie, J.U. (2006). An architectural framework that may lie at the core of the postsynaptic density. Science *311*, 531-535.

Contos, J.J., Ishii, I., Fukushima, N., Kingsbury, M.A., Ye, X., Kawamura, S., Brown, J.H., and Chun, J. (2002). Characterization of lpa(2) (Edg4) and lpa(1)/lpa(2) (Edg2/Edg4) lysophosphatidic acid receptor knockout mice: signaling deficits without obvious phenotypic abnormality attributable to lpa(2). Molecular and cellular biology *22*, 6921-6929.

Distler, U., Schmeisser, M.J., Pelosi, A., Reim, D., Kuharev, J., Weiczner, R., Baumgart, J., Boeckers, T.M., Nitsch, R., Vogt, J.*, et al.* (2014). In-depth protein profiling of the postsynaptic density from mouse hippocampus using data-independent acquisition proteomics. Proteomics *14*, 2607-2613.

Fan, W. (2013). Group I metabotropic glutamate receptors modulate late phase long-term potentiation in hippocampal CA1 pyramidal neurons: comparison of apical and basal dendrites. Neuroscience letters *553*, 132-137.

Geromanos, S.J., Vissers, J.P., Silva, J.C., Dorschel, C.A., Li, G.Z., Gorenstein, M.V., Bateman, R.H., and Langridge, J.I. (2009). The detection, correlation, and comparison of peptide precursor and product ions from data independent LC-MS with data dependant LC-MS/MS. Proteomics *9*, 1683-1695.

Kawauchi, T., Chihama, K., Nabeshima, Y., and Hoshino, M. (2003). The in vivo roles of STEF/Tiam1, Rac1 and JNK in cortical neuronal migration. The EMBO journal *22*, 4190-4201.

Krauss, M., Weiss, T., Langnaese, K., Richter, K., Kowski, A., Veh, R.W., and Laube, G. (2007). Cellular and subcellular rat brain spermidine synthase expression patterns suggest region-specific roles for polyamines, including cerebellar pre-synaptic function. Journal of neurochemistry *103*, 679-693.

Lujan, R., Roberts, J.D., Shigemoto, R., Ohishi, H., and Somogyi, P. (1997). Differential plasma membrane distribution of metabotropic glutamate receptors mGluR1 alpha, mGluR2 and mGluR5, relative to neurotransmitter release sites. J Chem Neuroanat *13*, 219-241.

Patzig, J., Jahn, O., Tenzer, S., Wichert, S.P., de Monasterio-Schrader, P., Rosfa, S., Kuharev, J., Yan, K., Bormuth, I., Bremer, J.*, et al.* (2011). Quantitative and integrative proteome analysis of peripheral nerve myelin identifies novel myelin proteins and candidate neuropathy loci. J Neurosci *31*, 16369-16386.

Postina, R., Schroeder, A., Dewachter, I., Bohl, J., Schmitt, U., Kojro, E., Prinzen, C., Endres, K., Hiemke, C., Blessing, M.*, et al.* (2004). A disintegrin-metalloproteinase prevents amyloid plaque

formation and hippocampal defects in an Alzheimer disease mouse model. The Journal of clinical investigation *113*, 1456-1464.
Prozorovski, T., Schulze-Topphoff, U., Glumm, R., Baumgart, J., Schroter, F., Ninnemann, O., Siegert, E., Bendix, I., Brustle, O., Nitsch, R.*, et al.* (2008). Sirt1 contributes critically to the redox-dependent fate of neural progenitors. Nature cell biology *10*, 385-394.
Rampon, C., Tang, Y.P., Goodhouse, J., Shimizu, E., Kyin, M., and Tsien, J.Z. (2000). Enrichment induces structural changes and recovery from nonspatial memory deficits in CA1 NMDAR1-knockout mice. Nature neuroscience *3*, 238-244.
Schmeisser, M.J., Ey, E., Wegener, S., Bockmann, J., Stempel, A.V., Kuebler, A., Janssen, A.L., Udvardi, P.T., Shiban, E., Spilker, C.*, et al.* (2012). Autistic-like behaviours and hyperactivity in mice lacking ProSAP1/Shank2. Nature *486*, 256-260.
Sholl, D.A. (1953). Dendritic organization in the neurons of the visual and motor cortices of the cat. J Anat *87*, 387-406.
Silva, J.C., Denny, R., Dorschel, C.A., Gorenstein, M., Kass, I.J., Li, G.Z., McKenna, T., Nold, M.J., Richardson, K., Young, P.*, et al.* (2005). Quantitative proteomic analysis by accurate mass retention time pairs. Anal Chem *77*, 2187-2200.
Tenzer, S., Docter, D., Rosfa, S., Wlodarski, A., Kuharev, J., Rekik, A., Knauer, S.K., Bantz, C., Nawroth, T., Bier, C.*, et al.* (2011). Nanoparticle size is a critical physicochemical determinant of the human blood plasma corona: a comprehensive quantitative proteomic analysis. ACS nano *5*, 7155-7167.
Tokumitsu, H., Hatano, N., Tsuchiya, M., Yurimoto, S., Fujimoto, T., Ohara, N., Kobayashi, R., and Sakagami, H. (2010). Identification and characterization of PRG-1 as a neuronal calmodulin-binding protein. Biochem J *431*, 81-91.
Trimbuch, T., Beed, P., Vogt, J., Schuchmann, S., Maier, N., Kintscher, M., Breustedt, J., Schuelke, M., Streu, N., Kieselmann, O.*, et al.* (2009). Synaptic PRG-1 modulates excitatory transmission via lipid phosphate-mediated signaling. Cell *138*, 1222-1235.
Vogt, J., Glumm, R., Schluter, L., Schmitz, D., Rost, B.R., Streu, N., Rister, B., Suman Bharathi, B., Gagiannis, D., Hildebrandt, H.*, et al.* (2012). Homeostatic regulation of NCAM polysialylation is critical for correct synaptic targeting. Cellular and molecular life sciences : CMLS *69*, 1179-1191.
Vogt, J., Yang, J.W., Mobascher, A., Cheng, J., Li, Y., Liu, X., Baumgart, J., Thalman, C., Kirischuk, S., Unichenko, P.*, et al.* (2016). Molecular cause and functional impact of altered synaptic lipid signaling due to a prg-1 gene SNP. EMBO molecular medicine.
Wisniewski, J.R., Zougman, A., Nagaraj, N., and Mann, M. (2009). Universal sample preparation method for proteome analysis. Nat Methods *6*, 359-362.